

4.0 HANGING WALL CRUSTAL VELOCITY STRUCTURE

The 3D velocity-hypocenter inversion (see Section 3) used 1150 earthquakes recorded by the Jackson Lake Seismic Network to delineate a 3-to-4-km-deep low-velocity “basin” in the hanging wall of the east-dipping Teton fault, but could not resolve details of the velocity structure portion of the hanging wall containing Jackson Lake Dam. Previous studies (Behrendt et al., 1968, Tibbetts et al., 1969; Byrd et al., 1994) used seismic refraction and gravity data to delineate a geophysical “basin” consisting of low-velocity (surface P-wave velocities of ~ 2.2 km/s), low-density (densities of 2.3 g/cm^3) Cenozoic and Mesozoic rocks. Low velocities in the hanging wall begin 1-2 km east of the surface scarp of the Teton fault, extend east of Jackson Lake Dam, and extend east of the likely eastern limit of the Teton fault at depth. The geophysical measurements of P- and S-wave velocities in the vicinity of the dam by Sirles (1986) provide the only direct measurements of S-wave velocities within the low-velocity portion of the hanging wall.

In this section, a low-velocity basin (LVB) in the hanging wall is defined in terms of its internal velocity properties, particularly the large impedance contrasts between the LVB and the surrounding high-velocity basement rocks, because these are the crustal properties that have the strongest influence on ground motion responses at the dam. The LVB extends beyond the geographic confines of the hanging wall located directly above the fault surface (compare Figure 4-1 to Plate 1), and encompasses a wide variety of stratigraphic units that happen to have similar velocities: All the sedimentary units in the LVB have velocities that are much lower than surrounding basement rocks. Although the LVB consists of Cenozoic and Mesozoic sedimentary stratigraphic units, designation of the LVB shown as in Figure 4-1 reflects long-standing geophysical practice (e.g., Boore, 1970, Boore et al., 1971), which focuses on defining the velocity (not stratigraphic) properties of the crust for the purposes of ground motion modeling. No attempt is made here to associate specific stratigraphic units with velocity features in the LVB, since this is not necessary for the purposes of ground motion estimation at the dam.

Rupture of the northern segment of the Teton fault for shallow dips of 35° and 45° would involve fault rupture directly beneath the dam (Figure 4-1). Thus, it is important to determine how strongly rupture directivity may influence peak ground motions and ground motion variability at

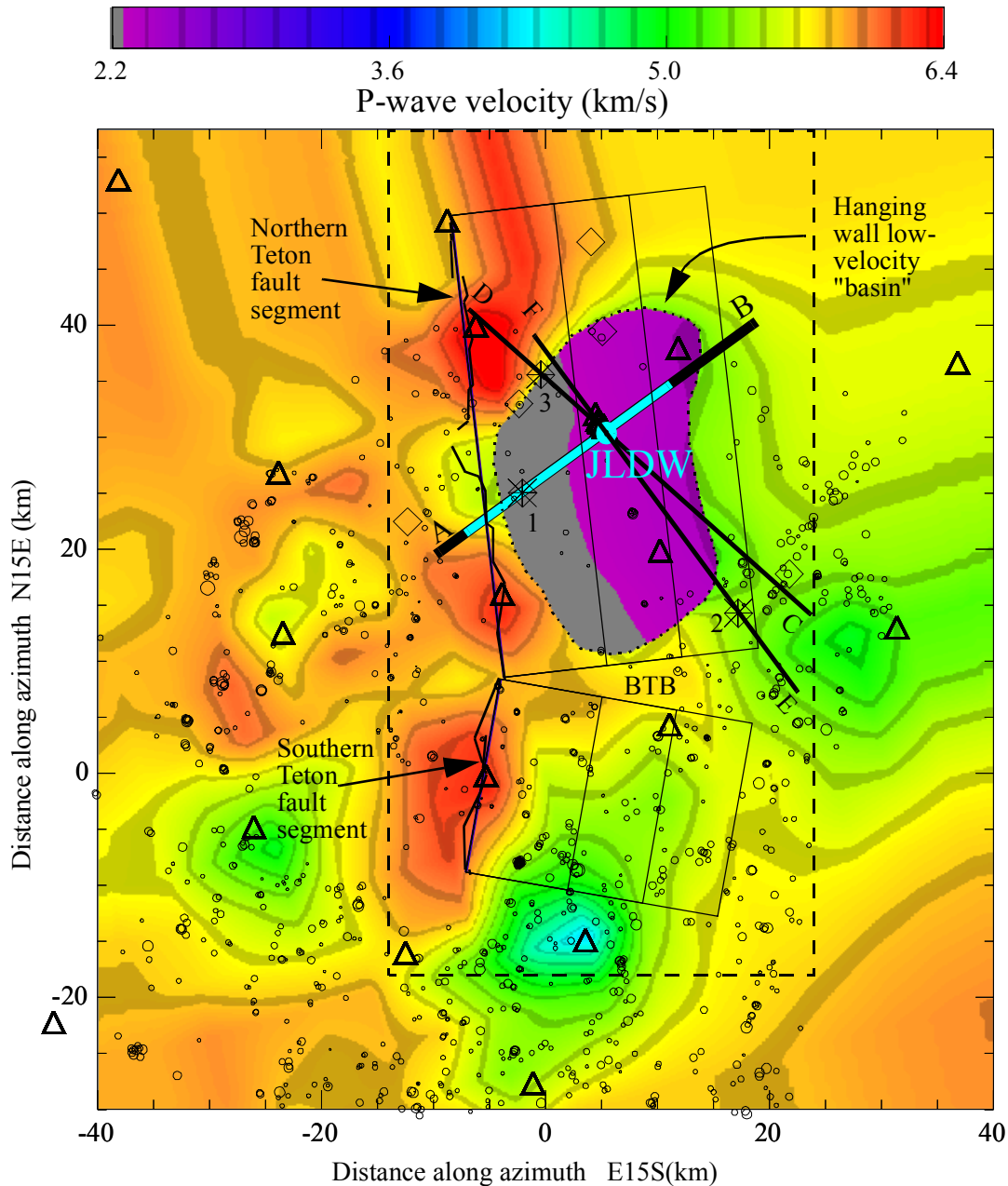


Figure 4-1: Plan view of the P-wave 3D velocity model with the embedded hanging wall LVB at 2 km elevation. The LVB is “closed”; it’s surrounded by high-velocities everywhere (in depth and plan views). Black circles are earthquake epicenters, triangles are JLSN seismographic stations, numbered stars show epicenters of the three earthquakes used for 2D finite-difference waveform modeling, and diamonds are empirical Green’s function (EGF) epicenters used in Section 6. The plan projection of the idealized geometries of the two primary (northern and southern) segments of the Teton fault for dips of 35°, 45°, and 60° are the solid rectangles (detailed surface scarps to the left are the short, irregular line segments). The 2D S-wave velocity cross section in Figure 4-4 is the thick black line labeled A -B (Figure 4-5 is the cyan portion of the line). Profile C-D corresponds to Figure 4-8 and profile E-F corresponds to Figure 4-11. Blue circle is the JLDW rock site station. The dashed rectangle shows the limits of the 3D finite-difference grid. Blacktail Butte is denoted by BTB.

the dam for these near-source earthquake scenarios. Impacts of 3D crustal velocity structure on ground motion amplitudes and durations are substantial (Frankel, 1993). Much of the modeling effort is devoted to accounting for the influences of 3D velocity heterogeneity, particularly hanging wall LVB velocity structure, on ground motion amplitudes and durations. It is necessary to constrain S-wave velocities within the hanging wall LVB to estimate ground motions at the dam. A mini-array of seven three-component digital broadband stations with a long-axis aperture of 1.6 km oriented along the axis of the dam was operated from October 1995 to May 2001 to record site responses within the Jackson Lake LVB, particularly on or near the dam. One site (station JLDW) was located near Signal Mountain, about 0.2 km south of the dam, on ~ 1 km/s S-wave-velocity over-compacted glacial till (Sirles, 1986) to serve as a “rock” reference site. However, because JLDW was located within the hanging wall LVB, it recorded secondary S-wave and surface wave arrivals originating at the LVB margins. Waveform modeling of direct S-waves and later secondary arrivals from microearthquake seismograms from the seven-station mini-array near the dam was used to constrain LVB S-wave velocities and LVB margin geometry. This section presents waveform and traveltimes modeling results used to constrain P- and S-wave velocities, and attenuation (Q_p and Q_s) characteristics within the hanging wall LVB to support rock and soil ground motion simulations presented in Section 6 and soil and site response investigations in Section 5.

4.1 3D Velocity Model Development Using Seismic Refraction Data.

LVB velocity structure was derived from the 3D velocity-velocity model (Section 3), reinterpretation of existing seismic refraction data, and 2D finite-difference waveform modeling of three microearthquakes (MEQ) located near the perimeter of the LVB, and recorded on broadband stations near the middle of the LVB. Four seismic refraction lines were shot in 1964 and 1965 by Behrendt et al. (1968) to study P-wave velocity structure in the LVB east of the Teton fault (e.g., Jackson Hole). Plate 1 from Behrendt et al. (1968) shows the shot and recording geometries of the seismic refraction lines. The recording geometries for lines 1-3 consisted of six geophone arrays with 0.5-km spacings between geophones (line 4 used 0.2-km spacings between geophones) and 1-3 km gaps in geophone coverage along the lines (Plate 1 and Figure 4-2).

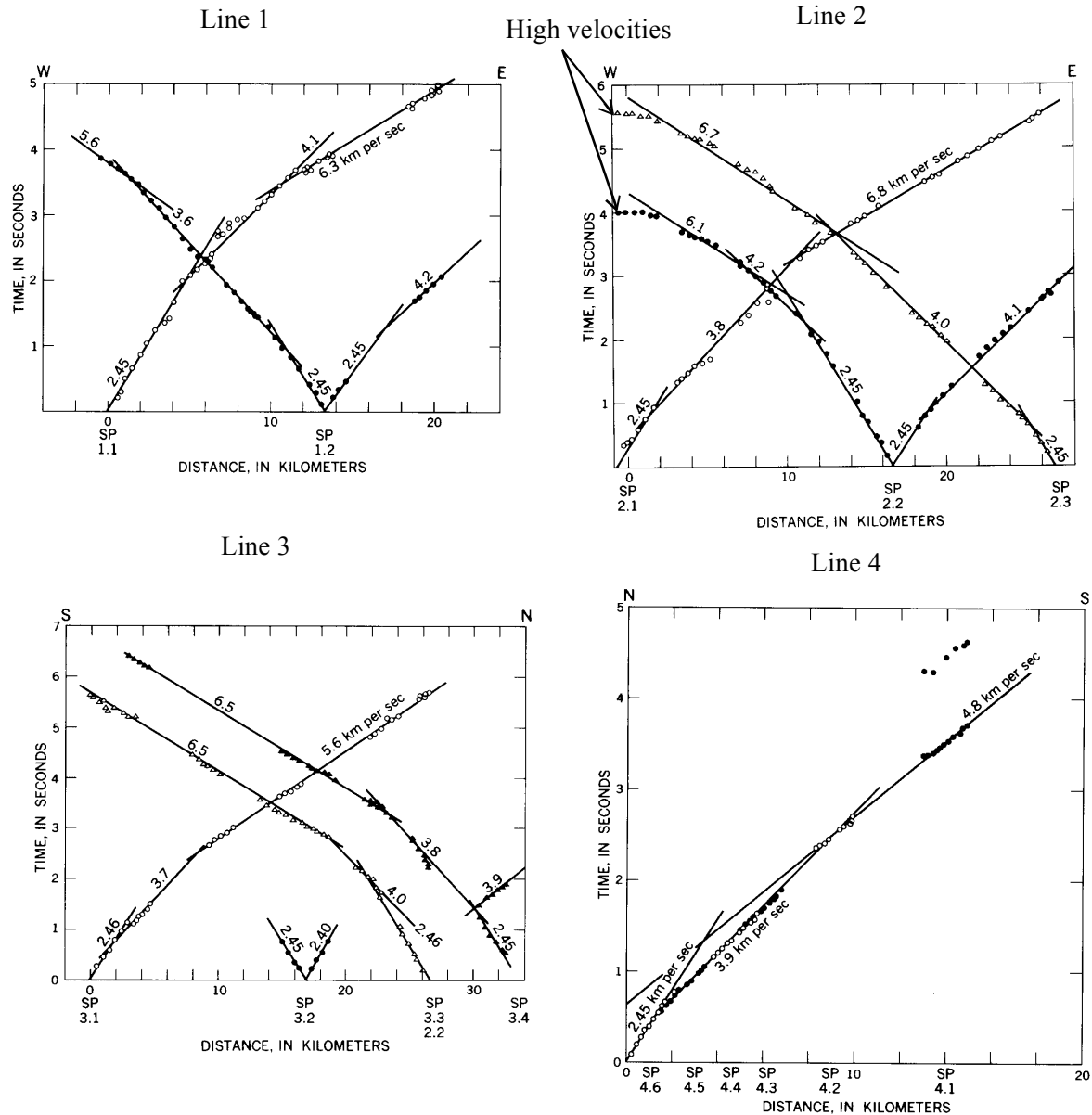


Figure 4-2: P-wave travel-time plots for lines 1-4 from Behrendt et al. (1968). The circles and triangles are the traveltimes observations and the straight line segments are the constant-velocity-layer velocity interpretations from Behrendt et al. (1968) labeled in km/s; SP are shotpoint numbers from Plate 1. Note that most traveltimes branches have 1-3 km traveltime gaps that make it impossible to distinguish between gradient and constant velocity layer interpretations of the traveltimes < 3 s (which constrain velocity structure within the LVB). The western portion of line 2, located ~1 km north of Jenny Lake, shows very-high apparent velocities for shotpoints 2.2 and 2.3 as show by the arrows.

There are three published traveltime interpretations of line 2 (Behrendt et al., 1968; Tibbetts et al., 1969; Byrd et al., 1994); none of these published interpretations included amplitude modeling of refraction data waveforms. Inevitably there are an infinite number of velocity models that can satisfy the traveltime data, but a finite class of velocity models that can satisfy band-limited amplitude data. This study attempts to satisfy the traveltime constraints represented by the seismic refraction data, but focuses on developing velocity models that reproduce the dominant < 4 Hz phases of three-component seismograms recorded in the interior of the LVB; producing a 3D velocity model that can reproduce ground motion observations most relevant to strong motions within the LVB is the focus of this investigation. In this subsection the seismic refraction interpretations are presented and discussed in relation to the 3D velocity model developed using LVB-edge MEQ seismograms in Section 4.2.

It is useful for illustration to start with the results of Behrendt et al. (1968). Behrendt et al. (1968) and Tibbetts et al. (1969) used forward modeling and delay-time analyses of line 2 travel times, and gravity modeling, to infer velocities and thicknesses of constant-velocity layers (Figure 4-3). Lines 1-3 have very crooked and discontinuous recording geometries (Plate 1). Consequently neither of the dip lines (lines 1 and 2) is normal to the structural strike and strike 3 is not parallel to structural strike (Plate 1). However, line 2 in particular, provides valuable constraints on the characteristics of the western boundary of the LVB. The very high apparent velocities on the western travel-time branch of shotpoint 2.2 (noted on Figure 4-2) unequivocally establishes that the LVB begins 1-2 km east of the surface scarp of the Teton fault, as discussed in detail below, and that there is a strong velocity contrast between LVB material and surrounding basement rocks. The reversed traveltime curves provided by shotpoints 2.1 and 2.2 place strong constraints on the maximum depth of the LVB. The initial slopes of the travel-times curves establish that the near-surface (depth) till P-wave velocities of 2.2-to-2.45 km/s measured by Sirles (1986) south of Jackson Lake Dam, are representative of shallow P-wave velocities throughout the LVB. This suggests that the near-surface till S-wave velocities of ~ 1.0 km/s measured by Sirles (1986) are also likely to be representative of near-surface till S-wave velocities throughout the LVB. Finally, it is clear from the seismic refraction data that P-wave velocities increase with depth, although the refraction lines are too crooked and discontinuous to make an unequivocally distinction between

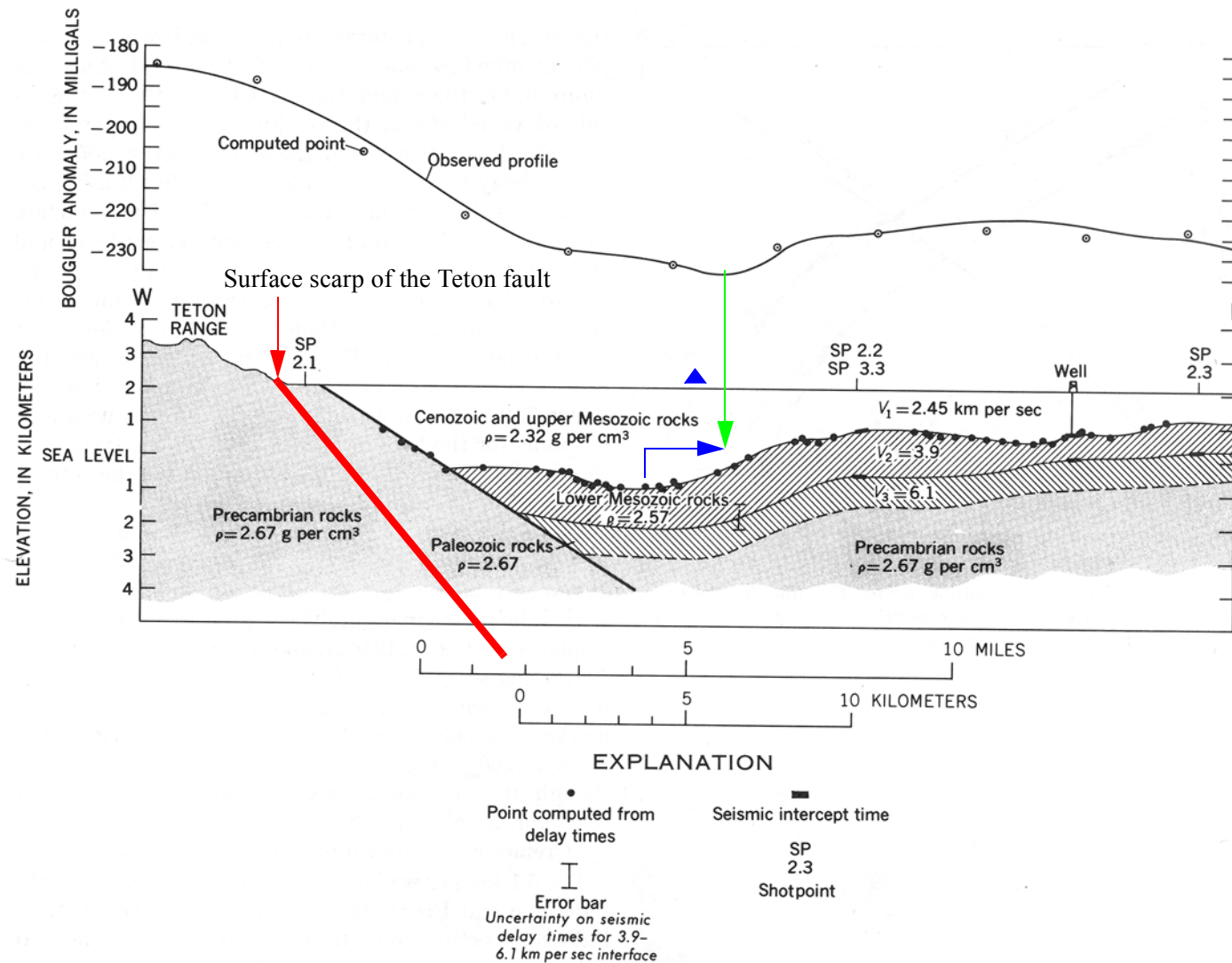


Figure 4-3: Line 2 gravity and seismic refraction interpretation reproduced from Behrendt et al. (1968). The red arrow and line show the approximate position of the surface scarp and depth (for an arbitrarily selected 50° dip) of the Teton fault (from Section 2), and the blue triangle shows the projected position of Jackson Lake Dam. The vertical green arrow indicates the minimum observed gravity location and the blue arrow points from where the maximum LVB depth is in the model to where the maximum LVB depth is indicated by the gravity data.

constant velocity and vertical-velocity-gradient interpretations of the traveltimes data. However, as shown in the next section, constant-velocity layers do not reproduce strong secondary arrivals observed on MEQ seismograms in the interior of the LVB.

Behrendt et al. (1968) assume the scatter in travel-times about fitted apparent velocities in Figure 4-2 is the result of variations in the thicknesses of the assumed constant velocity layers and use the delay time analysis method of Pakiser and Black (1957) to produce the detailed layer depth variation estimates of Figure 4-3. However, the gravity data in Figure 4-4 and Plate 1 indicate that the deepest portion of the LVB is likely located near or slightly east of Jackson Lake Dam, in contrast to the inferred LVB geometry inferred by Behrendt et al. (1968) in Figure 4-3. In contrast to Behrendt et al. (1968) and Tibbetts et al. (1969), Byrd et al. (1994) allowed velocity gradients in their ray-tracing velocity inversions of the traveltimes from line 2. They found evidence for vertical and horizontal velocity gradients. Unfortunately, Byrd et al. (1994) do not report the vertical or horizontal velocity gradients for their models, although from circular ray arcs in their Figure 9, it is clear that they found significantly non-zero vertical velocity gradients.

4.2 3D Velocity Model Development Using LVB Seismograms.

Three microearthquakes located near the perimeter of the LVB (Figure 4-1) were recorded by the site-response stations in the vicinity of Jackson Lake Dam. Signal-to-noise levels in the seismograms were adequate to use the seismograms in trial-and-error waveform modeling to constrain P- and S-wave velocity structure within the LVB. Earthquakes located close to the perimeter of the LVB were selected because they produced strong secondary arrivals associated with secondary S-waves and surface waves generated at the large-velocity contrast between the low-velocity sediments and surrounding basement rocks. The 2D version of the elastic finite-difference program E3D (Larsen and Grieger, 1998), which includes viscoelastic capabilities implemented using the approach of Robertsson et al. (1994), was used to calculate the seismic response of a double-couple point source for 2D velocity slices intersecting the earthquakes and station JLDW. The JLSN provided the earthquake location and focal mechanism constraints necessary to minimize trade-offs between velocity structure, earthquake locations, and focal mechanisms. Grid spacings of 0.032 km were used to allow modeling of seismograms to a maximum frequency of 4 Hz given minimum S-wave velocities of ~ 1 km/s (> 6 points per

wavelength sampling at 4 Hz to minimize grid dispersion in a fourth-order finite-difference code, e.g., Moczo et al., 2000). The observed seismograms were rotated to provide a radial horizontal component seismogram to compare with synthetic radial seismograms from the 2D P-SV finite-difference modeling. The observed seismograms were low-pass-filtered at the lowest possible frequencies as allowed by signal-to-noise levels, to focus on fitting seismogram frequencies most likely to be strongly influenced by 3D deterministic velocity structure; as frequencies increase above 5 Hz, seismogram coherence is expected to decrease substantially because velocity heterogeneity in the crust (Frankel and Clayton, 1986) strongly perturbs body-wave phase as the mean free path increases (Spetzler and Snieder, 2001). The 2D synthetic seismograms are corrected using the approach of Vidale and Helmberger (1987) to approximate a point-source and corresponding 3D geometric spreading.

The velocity inversion results of Byrd et al. (1994) suggested that linear-velocity-gradient models for the LVB were most consistent with the seismic refraction data. Consequently, the trial-and-error forward modeling effort focused on developing linear-velocity-gradient velocity models for the LVB embedded in the 3D velocity model obtained from a progressive velocity-hypocenter inversion (Section 3, Figure 4-1). Constant-velocity-layer models similar to Behrendt et al. (1968) were also evaluated. One of the modeling requirements was to develop relationships to predict S-wave velocities, densities, Q_p , and Q_s , based on P-wave velocities. The model relationships used with the P-wave model in Figure 4-1 are shown in Table 4-1.

4.2.1 Synthetic Seismogram Modeling of the 19 April 2001 M 1.4 Earthquake. This earthquake occurred beneath the western margin of the LVB about 3.2 km below the surface (event 1 on Figure 4-1). First-motions from the JLSN indicate a normal-faulting focal mechanism with dips of 40-50 degrees for the east-dipping nodal plane. As indicated in Figure 4-4, depth uncertainties of ~1 km allow for Teton fault dips of 35-60 degrees, assuming the earthquake is located on the Teton fault. A small horizontal velocity gradient that makes the western-most LVB velocities 10% slower than the eastern-most LVB velocities was imposed to produce the minimum velocities along the western margin of the LVB in the 3D velocity model (Figures 4-1 and 4-4). The geometry of the LVB is similar to Behrendt et al.'s (1968) in Figure 4-3, but the deepest portion of the LVB is allowed to extend several km further east beneath the dam,

Table 4-1: Best-Estimates of Relationships between P-wave Velocity and Vs, ρ , Qp, and Qs.

Let V_p = P-wave velocity (km/s),
 $V_{p \max}$ = Maximum P-wave velocity in the 3D model (km/s),
 $V_{p \min}$ = Minimum P-wave velocity in the 3D model (km/s),
 $V_{p \text{ range}} = V_{p \max} - V_{p \min}$ (km/s),
 V_s = S-wave velocity (km/s),
 $V_p/V_{s \max}$ = Maximum V_p/V_s ratio in the 3D model = 2.2,
 $V_p/V_{s \min}$ = Minimum V_p/V_s ratio in the 3D model = 1.73,
 $V_p/V_{s \text{ range}} = V_p/V_{s \max} - V_p/V_{s \min} = 0.47$,
 ρ = density (g/cm^3),
 Q_p = P-wave attenuation quality factor,
 Q_s = S-wave attenuation quality factor,

Then:

$$V_s = V_p / \left[\left((V_{p \max} - V_p) / V_{p \text{ range}} \right)^3 * V_p/V_{s \text{ range}} + V_p/V_{s \min} \right],$$

$$\rho = (V_{p \max} - V_p) / V_{p \text{ range}} * -0.45 + 2.75,$$

$$Q_p = (V_{p \max} - V_p) / V_{p \text{ range}} * 350 + 50,$$

$$Q_s = (V_{s \max} - V_s) / V_{s \text{ range}} * 180 + 20.$$

These relationships were used to generate Vs, ρ , Qp, and Qs for the "best-fitting" 2D finite-difference grids in this section and the 3D finite-difference grids used to calculate ground motions in Section 6.

consistent with the gravity observations in Figure 4-3 and Plate 1. The 2D synthetic seismograms reproduces the relative amplitudes and travel-times of the direct P- and S-waves and the LVB-edge S-wave (Figure 4-5). Several Vs, Qp, and Qs relationships with P-wave velocity were tested before arriving at the relationships listed in Table 4-1. The synthetic seismogram also does a reasonable job of reproducing the total duration of ground motion; a relatively low Qs of 20 is used near the surface to reproduce observed durations and amplitude decays observed at JLDW.

A synthetic radial-component record section is shown in Figure 4-6 to illustrate the characteristics of the LVB-edge S-wave observed at station JLDW. The largest amplitudes are found in the western portion of the LVB closest to the hypocenter. However, the LVB-edge S-wave attains a peak velocity at the dam of 33% of the maximum velocity observed on the surface. These large LVB-edge S-wave amplitudes occurs at the dam because the dam is located ~10 km from the western LVB margin, in the distance range where a caustic develops due to the critical refraction/reflection of the LVB-edge S-wave along the east-dipping margin of the western LVB. Using JLDW as the source position and invoking reciprocity, the ray paths in Figure 4-7b illustrate the consequences of the geometry of the western margin of the LVB on ground motion amplification at the dam. Refraction/reflection along the western LVB boundary produces focusing (e.g., near zero wavefront curvature) that counteracts geometric spreading sufficiently to make the LVB-edge S-wave amplitude larger than the direct S-wave, even though the LVB-edge wave has propagated along a path distance that is nearly twice the propagation distance of the direct S wave. Figure 4-7a shows that the LVB captures radiated seismic energy over a very wide cross section. Thus, the LVB is a very efficient seismic collector, and sites within the LVB are likely experience substantial multipathing for sources located beneath the LVB (e.g., the Teton fault).

4.2.2 Synthetic Seismogram Modeling of the 29 Sep. 1996 M 1.6 Earthquake. This earthquake is located about 7 km northwest of station JLDW (the epicenter is event 3 in Figure 4-1) at a depth of 5-6 km (Figure 4-8). First-motions from the JLSN indicate a normal-faulting focal mechanism with dips of 47 degrees for the east-dipping nodal plane. Depth uncertainties of ~1 km allow for Teton fault dips of 40-50 degrees, assuming the earthquake is located on the Teton fault. The small magnitude and substantial long-period site noise required modeling to a maximum

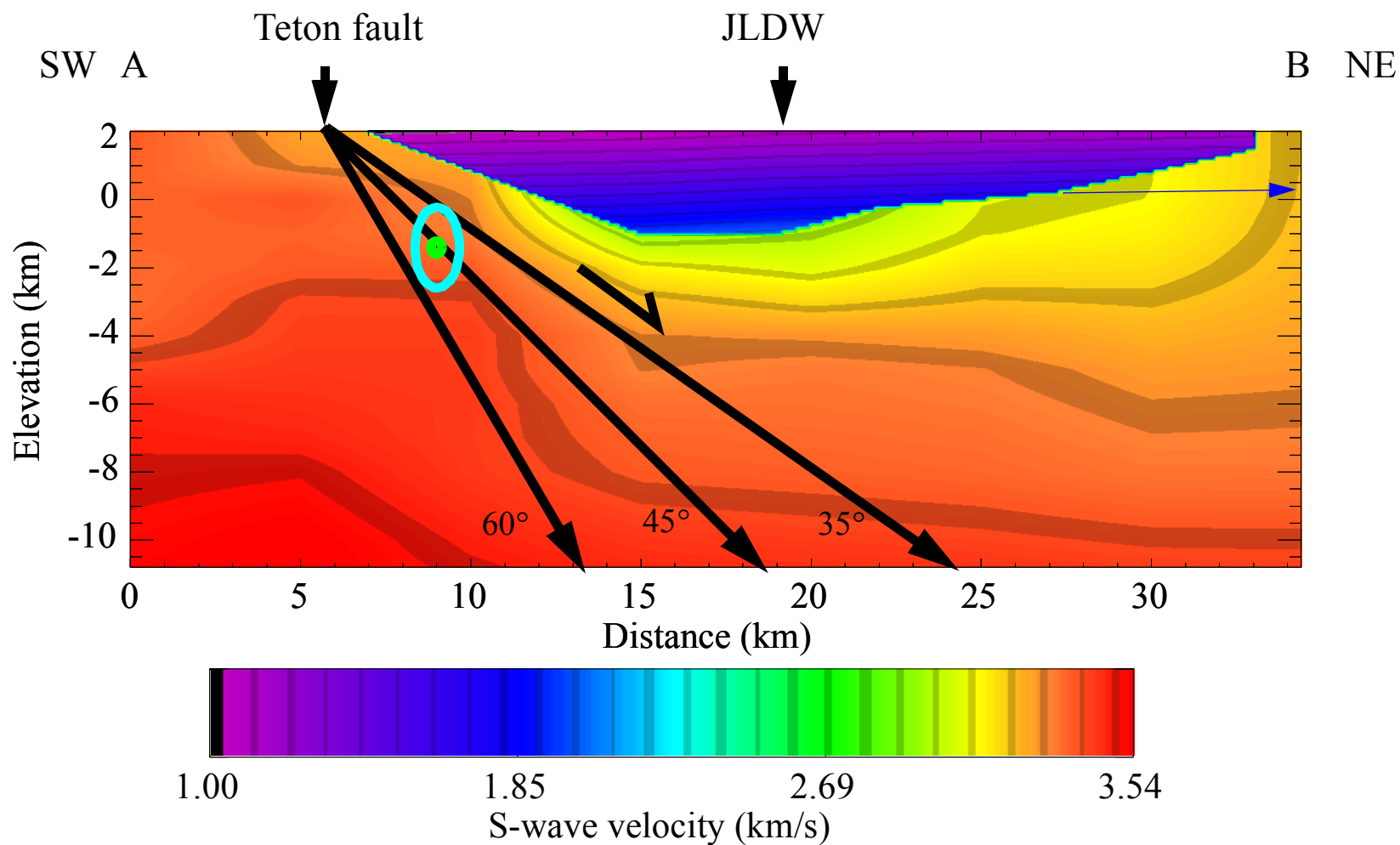


Figure 4-4: S-wave velocity depth cross section A-B (see Figure 4-1). The model was derived from trial-and-error *P-SV* 2D finite-difference waveform modeling of the observed rock-site radial seismogram from the 19 April 2001 **M** 1.4 earthquake (Figure 4-5). The hypocenter is the green circle and the cyan ellipse shows the hypocenter location uncertainty. The range of allowable dips for the Teton fault are indicated by the black arrows labeled 35° and 60°; a black arrow labeled 45° is also provided. Note that the LVB is located ~1-2 km east of the surface scarp of the Teton fault. Seismic refraction data and gravity data clearly establish that a shallow high-velocity (*P*-wave velocities > 6 km/s) and high-density body (> 2.6 g/cm³) is located between the Teton fault scarp and the LVB (Behrendt et al., 1968; Tibbetts et al., 1969; and Byrd et al., 1994). The blue arrow indicates that low velocities probably continue to the northeast with thicknesses of ~2 km.

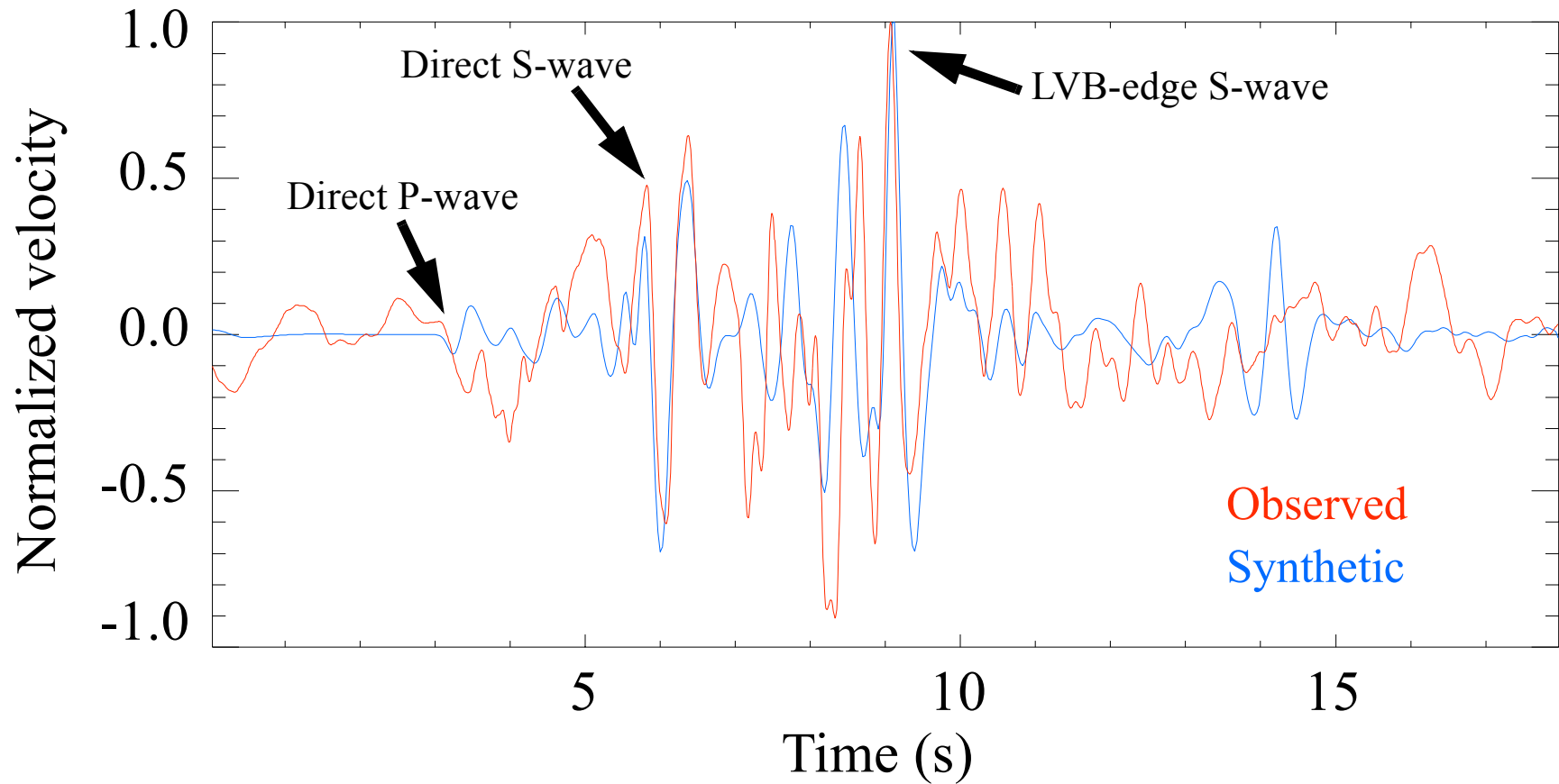


Figure 4-5: Radial-component JLDW seismogram from the **M** 1.4 normal-faulting earthquake on 19 April 2001. Seismograms are band-pass filtered from 0.5 Hz to 2 Hz; observed in red and synthetic in blue. This earthquake was located at a depth of 3.2 km below the LVB margin (epicenter is event 1 on Figure 4-1). The LVB-edge arrival from the western margin of the LVB is a critically reflected/refracted *S*-wave as indicated in the synthetic radial component record section in Figure 4-6 and by the rays in Figure 4-7. This secondary *S*-wave arrival is the largest amplitude arrival at this site and has an amplitude 33% of the largest *S*-wave amplitude recorded within the LVB, even though the JLDW rock site is located ~10 km from the western-edge of the LVB.

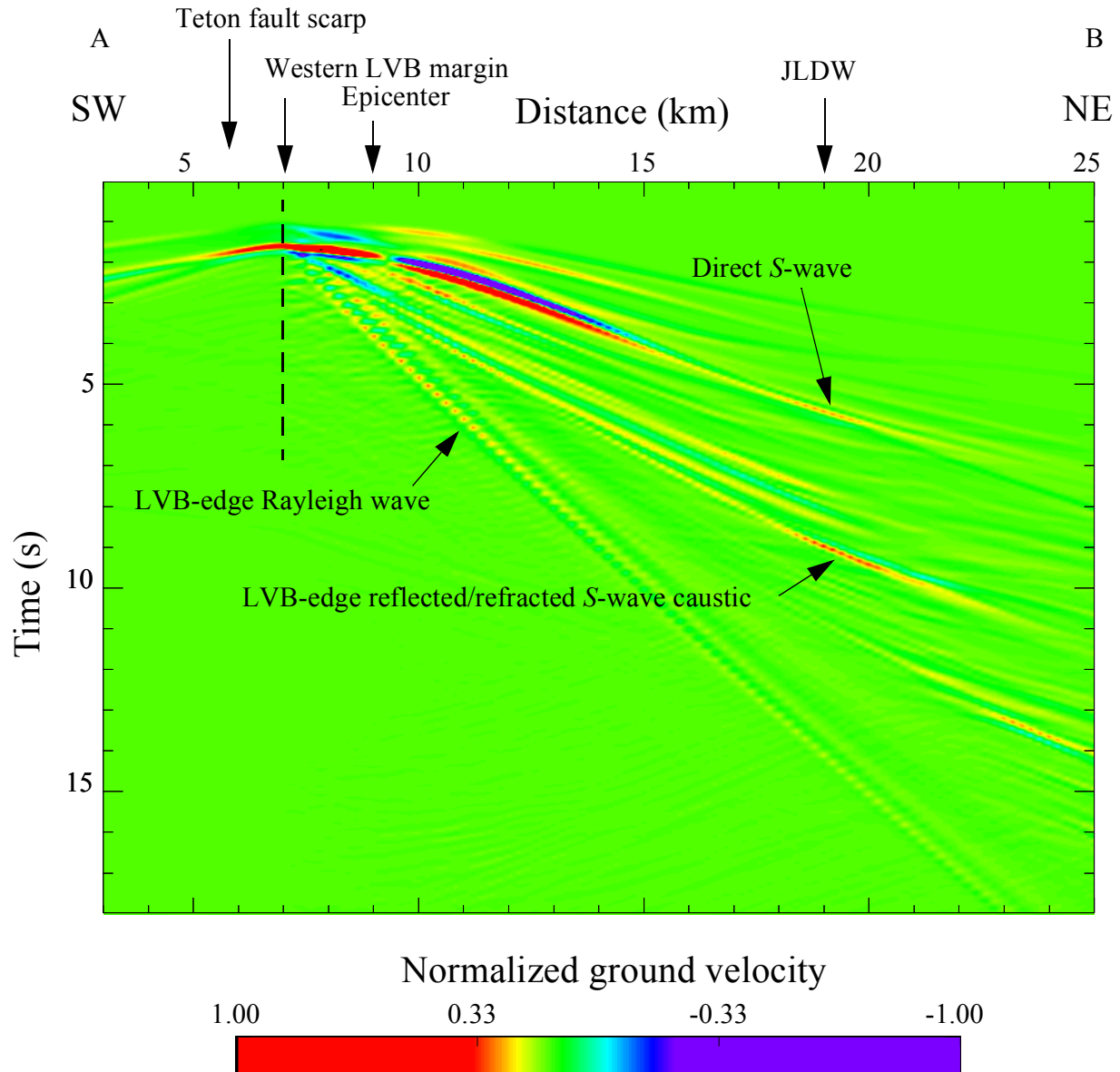


Figure 4-6: Synthetic radial-component-seismogram record section for the 19 April 2001 earthquake.

The record section has the same orientation as Figure 4-4 and is represented by the cyan portion of A-B in Figure 4-1. Labels and arrows show the locations of the rock site, epicenter, and surface scarp of the Teton fault. Note the secondary S-wave and surface wave arrivals generated at the western LVB edge (denoted by the dashed vertical line).

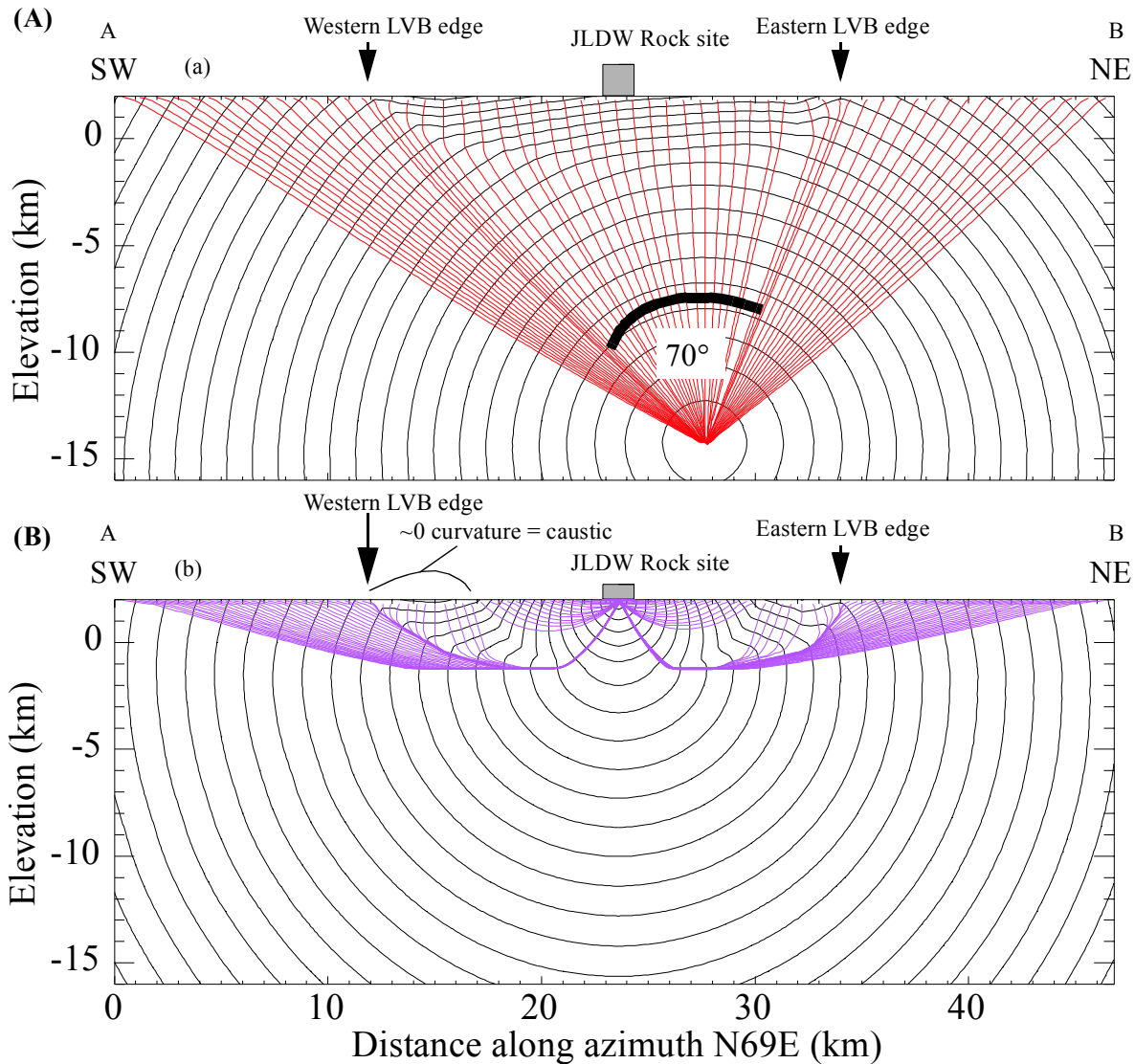


Figure 4-7: 2D ray-tracing slices through the 3D S-wave velocity model. (A) Black curves are isochrones and red curves are S-wave first-arrival ray paths from a hypocenter near the bottom of the Teton fault and east of the rock site (filled square). Rays emitted over a 70° arc from the source are captured by the LVB. (B) Purple rays are first S-wave arrivals from JLDW to positions within and outside the LVB (a reciprocity visualization). Note the first-arrival path between the western LVB-edge and the rock site is a refracted path along the large-velocity discontinuity between the LVB and the high-velocity basement rocks. Figure 4-6 shows large amplitudes associated with a triplication caustic for LVB-edge S-waves propagating to sites located between 9-11 km from the western margin of the LVB. The isochrone on the ~5-km-wide region on the western margin of the LVB has nearly zero curvature resulting in a caustic at the dam.

frequency of 4 Hz to obtain sufficient signal-to-noise ratios to model the direct S-wave and LVB-edge S-wave arrivals. The focus for modeling this earthquake was on varying the northwestern boundary dip and position (Figure 4-8), so no attempt was made to model the southeastern portion of the model in Figure 4-8, since it had little effect on the JLDW seismograms for this earthquake.

This is an important earthquake because it occurs close to line 4 of Behrendt et al. (1968) and provides constraints on the geometry of the northwestern boundary of the LVB (Plate 1 and Figure 4-9). The strongest lateral gravity gradient is located along the northwest boundary of the LVB (Plate 1 and Figure 4-9b). As noted by Behrendt et al. (1968), this requires the northwest LVB boundary to have a steep dip and for the LVB to have its maximum depth within the northwestern portion of the LVB (Figure 4-8). Several LVB boundary dips were used to calculate synthetic seismograms, only velocity models with steep LVB boundary dips were able to reproduce the observed amplitude ratios and time-differences between the direct S-wave and the LVB-edge S-wave on the radial seismogram (Figure 4-10).

Several Hertz reverberations persist for > 20 s in the observed seismograms (Figure 4-10). Frankel and Clayton (1986) showed that correlated-random (fractal) crustal velocity variations are necessary to explain seismic coda. To ascertain the importance of short-wavelength correlation on the waveform duration, a 2D fractal velocity randomization of the low-velocity-LVB portion of Figure 4-8 was employed using an anisotropic von-Karman autocorrelation function in the wavenumber domain, $P(k_r)$, of the form

$$P(k_r) \approx \frac{a_z a_x}{\left((a_z k_z)^2 + (a_x k_x)^2 \right)} \quad (4-1)$$

where a_x and a_z are the horizontal and vertical correlation distances, respectively, and k_x and k_z are the horizontal and vertical wavenumbers, respectively. Values of $a_x = 0.5$ km and $a_z = 0.35$ km were used because the deposits in the LVB are likely to vary more rapidly in depth than in the horizontal dimension (e.g., normal to bedding structures). A standard deviation of 9% was used which produced very long synthetic high-frequency coda durations (Figure 4-10). This suggests that either the actual velocity variability is better represented by standard deviations $< 9\%$ and/or that near-surface Q_s is < 20 . Since empirical Green's function were used to represent > 1 Hz site

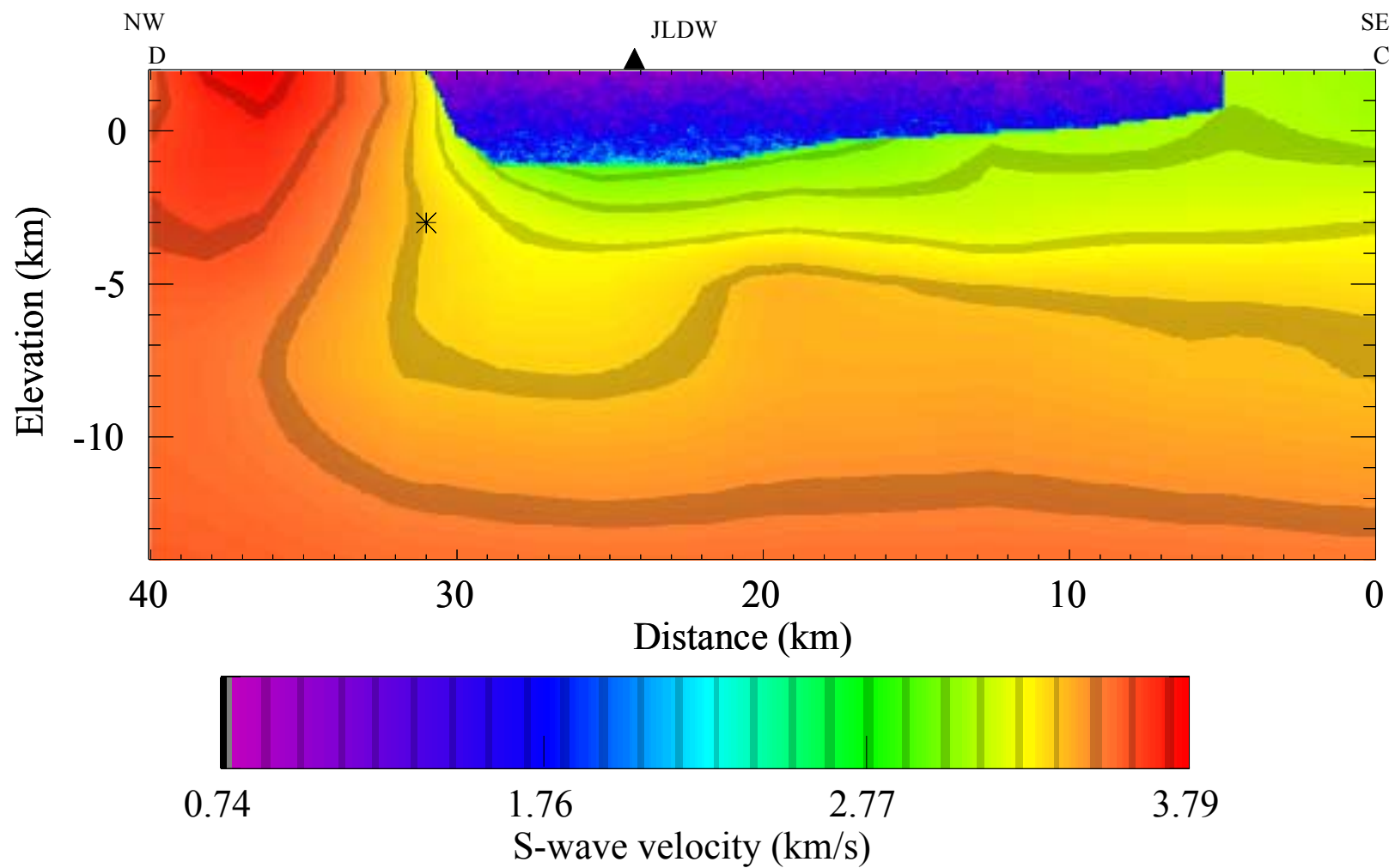


Figure 4-8: S-wave velocity-depth cross section C-D (see Figure 4-1) used to model the 29 Sep. 1996 **M** 1.6 earthquake. The hypocenter is the black star and station JLDW is the black triangle.

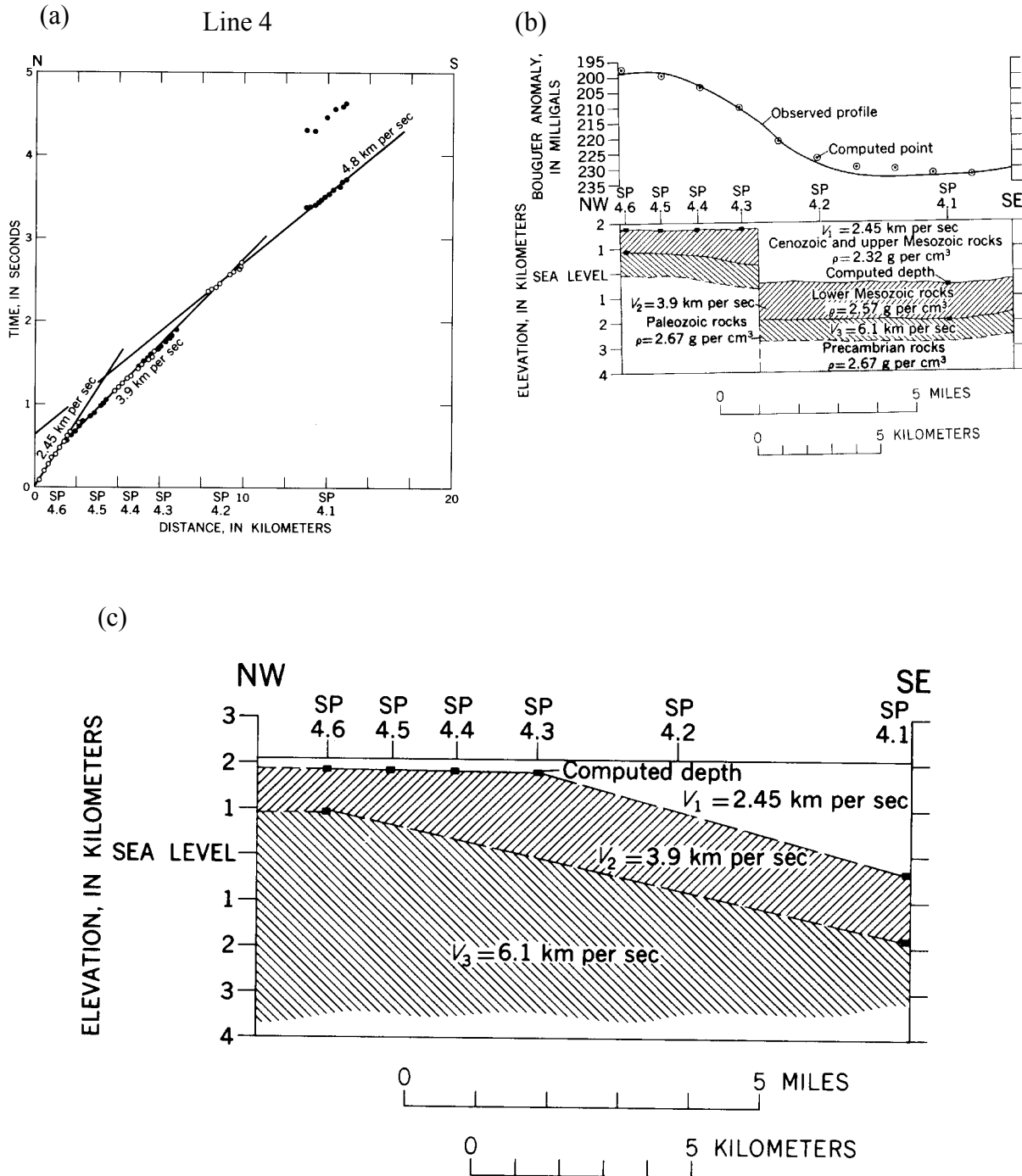


Figure 4-9: Line 4 traveltimes and interpretations reproduced from Behrendt et al. (1968). (a) Unreversed traveltimes from line 4 (see Plate 1 for shotpoint locations). (b) Behrendt et al.'s (1968) Bouguer-anomaly observations and 2D line integral gravity model for line 4 based on the model in (c). (c) P-wave velocity model from Behrendt et al. (1968) estimated using time-depth method and velocities from lines 1-3.

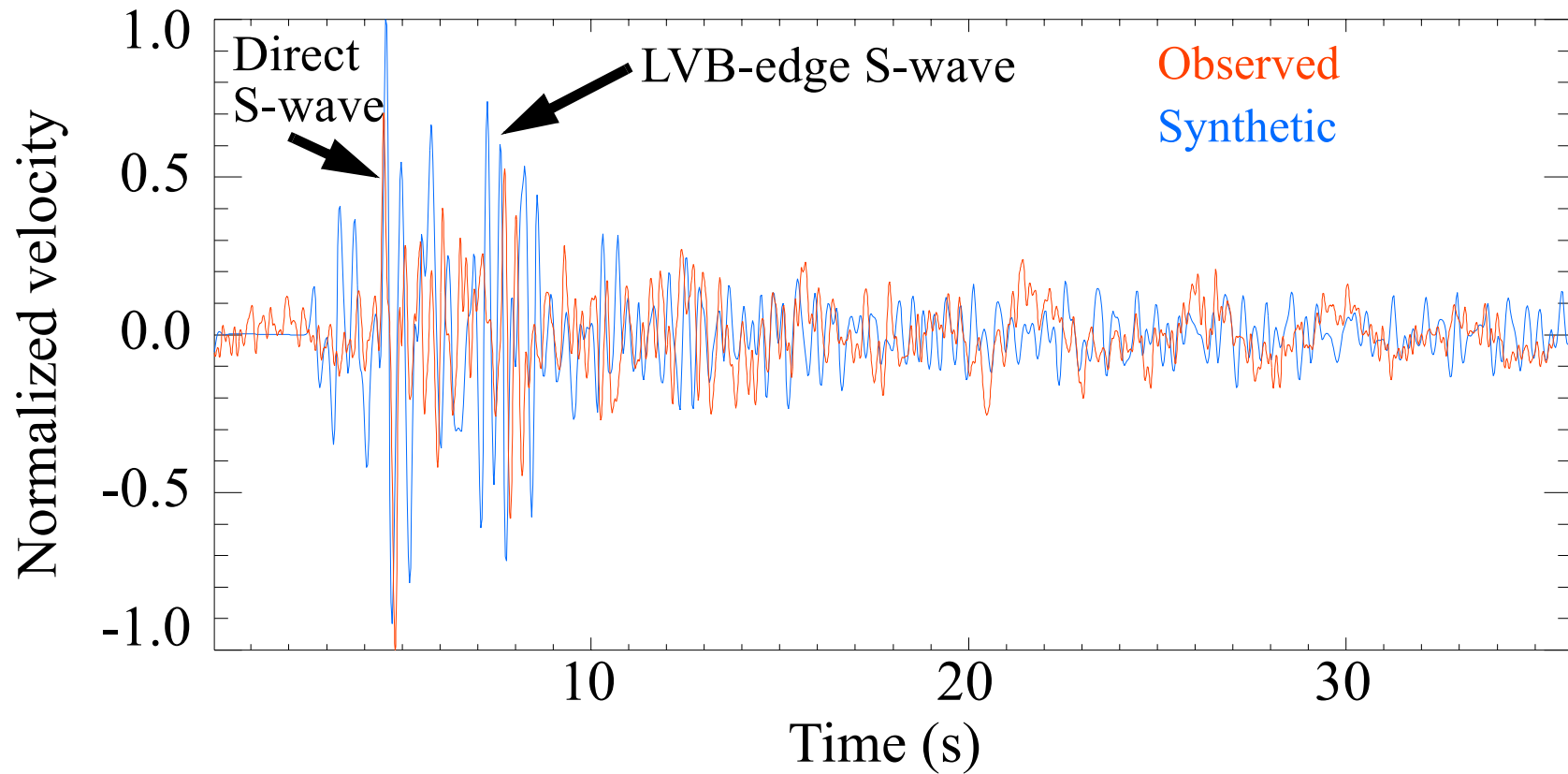


Figure 4-10: Radial-component JLDW observed seismogram from the **M** 1.6 normal-faulting earthquake on 29 Sep. 1996. The epicenter is event 3 on Figure 4-1. This earthquake was located at a depth of 6 km below the northwest portion of the LVB margin. Both the observed and synthetic seismograms were band-pass filtered from 0.5 Hz to 4 Hz. The amplitude of the secondary *S*-wave arrival is smaller than the direct *S*-wave arrival because the site is located about 6 km from the LVB edge closest to the hypocenter, too close to develop a critically reflected/refracted *S*-wave at the site. Because of long-period site noise and relatively small event magnitude, it was necessary to model to a maximum frequency of 4 Hz. In contrast to Figures 4-4, a 9% standard deviation fractal randomization of the velocities in the LVB was used to modify the 2D velocity model. This resulted in synthetic high-frequency durations more consistent with the observed data.

responses in Section 6, further comparisons of correlated-random velocity variations and variability of synthetic seismogram responses were not pursued.

4.2.3 Synthetic Seismogram Modeling of the 15 Nov. 2001 M 2.9 Earthquake. This earthquake is located about 20 km SSE of station JLDW (the epicenter is event 2 in Figure 4-1) at a depth of ~8 km (Figure 4-11). P-wave first-motions from the JLSN indicate an oblique-normal-faulting focal mechanism with a dip of 57 degrees for the east-dipping nodal plane. This earthquake is located too far east of the surface trace of the Teton fault to be associated with the fault. The magnitude of 2.9 allowed for modeling to lower frequencies (< 1.5 Hz) than the other two events. The focus for modeling this earthquake was on varying the southeastern boundary dip and position (Figure 4-11), so no attempt was made to model the northwestern portion of the model in Figure 4-11, since it had little effect on the JLDW seismograms for this earthquake. This model was developed prior to the modeling presented in Section 4.2.2.

The synthetic 2D seismogram provides good amplitude agreement with the observed direct S-wave and LVB-edge S-wave; the synthetic LVB-edge surface wave amplitude is a bit smaller than the observed amplitude (Figure 4-12). The synthetic LVB-edge S-wave arrives about 0.5 s later than the observed LVB-edge S-wave, but the synthetic and observed direct S-waves and LVB-edge surface waves arrival times are the same. Minor adjustments to the hypocenter location would likely reduce the arrival time discrepancies. Overall, the good agreement between the amplitudes of the observed and synthetic radial seismograms in Figure 4-12 indicates that the position and dip of the southern LVB margin in Figure 4-11 and the LVB velocities between the southeastern LVB margin and station JLDW are reasonable. The 9% standard deviation fractal velocity randomizations within the LVB imposed in the same manner as the 29 Sep. 1996 earthquake modeling increased synthetic durations. However, the synthetic duration is shorter than the observed duration, which probably reflects the lack of 3D multipathing in the 2D model, and the greater distance of this earthquake (> 20 km) from JLDW relative to the 29 Sep. 1996 earthquake (~7 km from JLDW). Durations using the 3D model are more consistent with the observed data as discussed in Section 4.4.

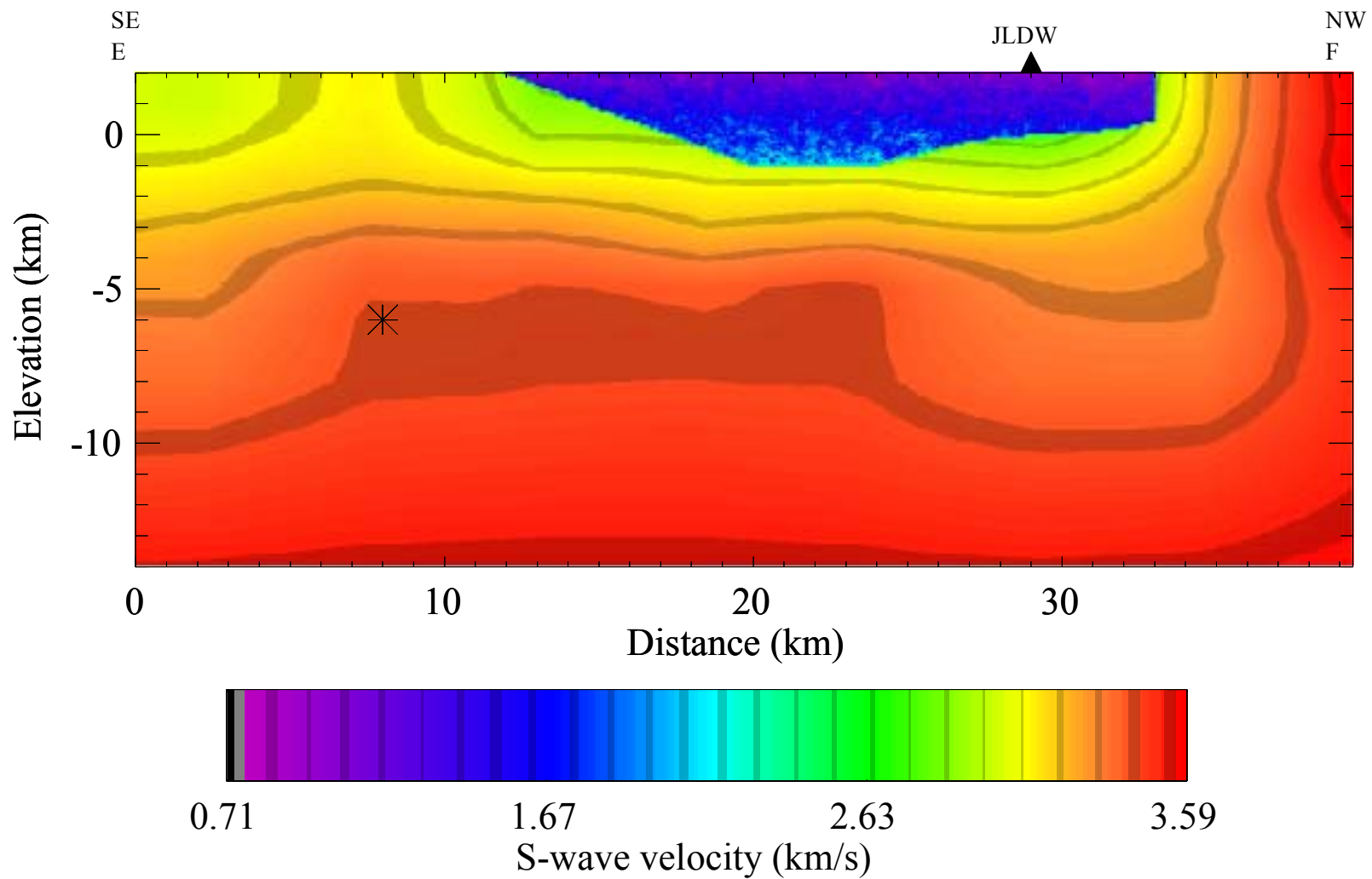


Figure 4-11: S-wave velocity-depth cross section E-F (see Figure 4-1) used to model the 15 Nov. 2001 **M** 2.9 earthquake. The hypocenter is the black star and station JLDW is the black triangle.

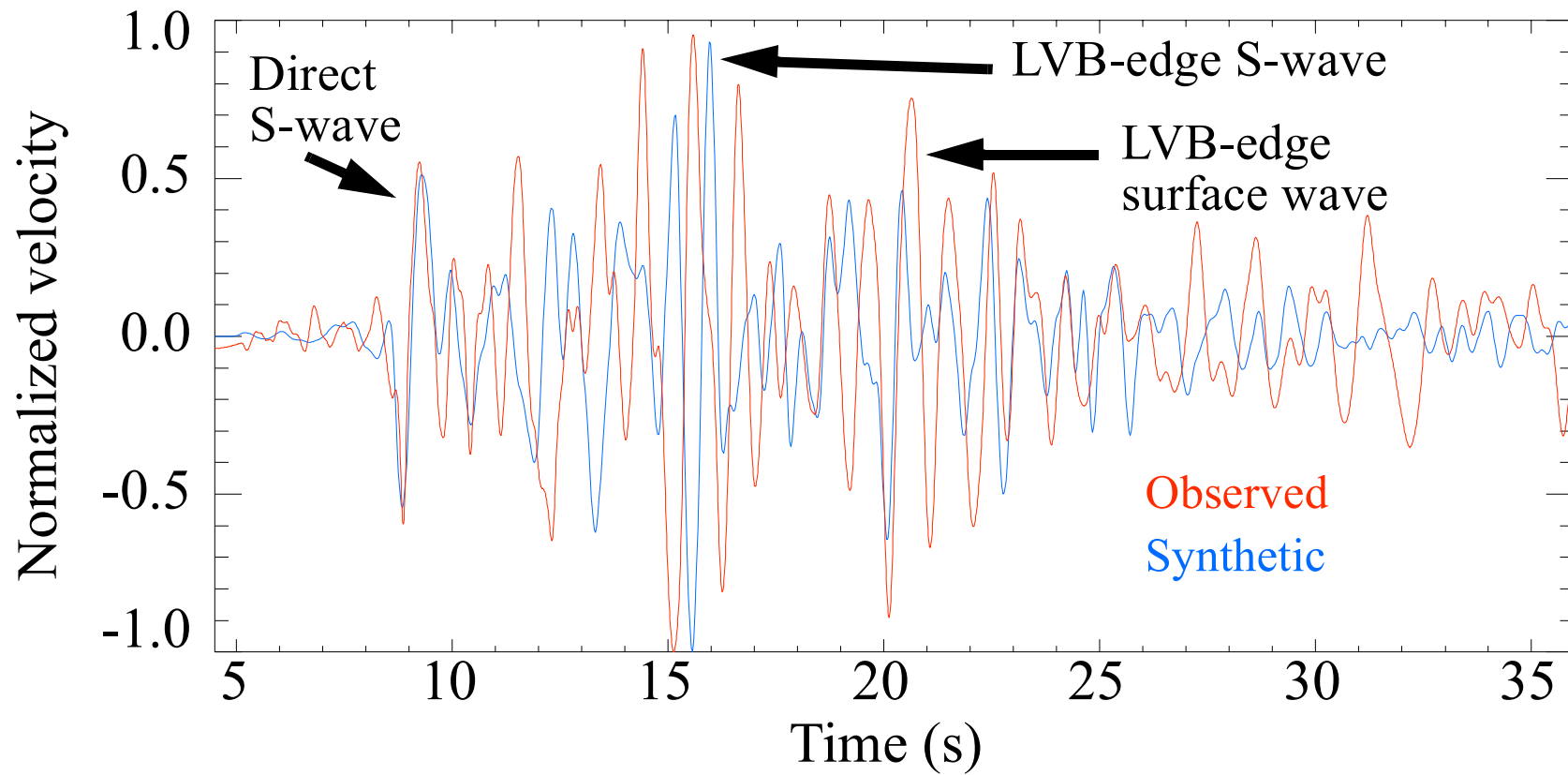


Figure 4-12: Observed and synthetic radial-component JLDW seismograms the **M** 2.9 normal-faulting earthquake on 15 Nov. 2001. (Epicenter is star 2 on Figure 4-1. Both seismograms were band-pass filtered from 0.5 Hz to 1.5 Hz. This earthquake was located at a depth of 8 km, within 4 km of the southeast corner of the LVB margin. Both the LVB-edge S-wave and the LVB-edge surface wave amplitudes are larger than the direct S-wave and are reasonably well reproduced by the blue 2D synthetic seismogram. The 2D velocity model does not reproduce the extended duration of the surface waves observed after 30 s. In contrast, the 3D finite-difference Green's functions include the multipathing necessary to reproduce observed durations (see Figures 4-18 and 4-19).

4.3 Comparison of 3D Velocity Model to the Seismic Refraction Data

The 3D P-wave velocity model reproduces the line 2 P-wave traveltimes of Behrendt et al. (1968) well, except for the eastern portion of the travel time data (Figure 4-13), where it is clear that the low-velocities would need to be continued to the east in the 3D model to match the refraction data. The truncation of the LVB east of the dam in the 3D velocity model is probably not a substantial issue for using the 3D model to estimate ground motions at the dam because the Teton fault interacts most strongly with the western portion of the LVB. However, it would be prudent to use several earthquakes located east of the dam recorded at station JLDW to constrain the eastward extent of the LVB.

The 3D velocity model produces a refracted traveltime branch on the west of shotpoint 2.1 that is about 0.1 s too late. As shown in Figure 4-14b, the bottom of the western portion of the LVB is probably 0.2-0.3 km too deep to precisely reproduce the traveltimes in the 2-10 km distance range in Figure 4-13. While the 3D velocity model actually fits the high apparent velocities observed for distances < 2 km in Figure 4-13, the model lacks the 0.1-0.2(?) km thickness of low-velocity near-surface material (moraines, talus, etc.) that likely comprise the near-surface materials between the LVB and the scarp of the active Teton fault. If the depths to the bottom of the western portion of the LVB in the 3D model were modified to reproduce the travel-time curve more closely in the 2-to-10-km distance range, the veneer of low-velocity near-surface materials that probably exist for distances < 2 km would also need to be added to the 3D velocity model to reproduce the observed shotpoint 2.2 western-branch traveltime curve in the < 10 km distance range. Since a grid spacing of 0.2 km was used in the 3D velocity model to calculate ground motions at the dam, these discrepancies in traveltimes all approach the resolution limit of the discrete 3D velocity model and are probably not significant for calculating < 1 Hz synthetic ground motion responses at the dam.

The 3D velocity model has a horizontal velocity gradient that increases velocities in the eastward direction. Whereas Behrendt et al. (1968) substantially decreased the thickness of low-velocity sediments east of JLDW, the 3D velocity model simply increases the average velocities of the sediments eastward, instead of decreasing sediment thicknesses eastward as rapidly as Behrendt

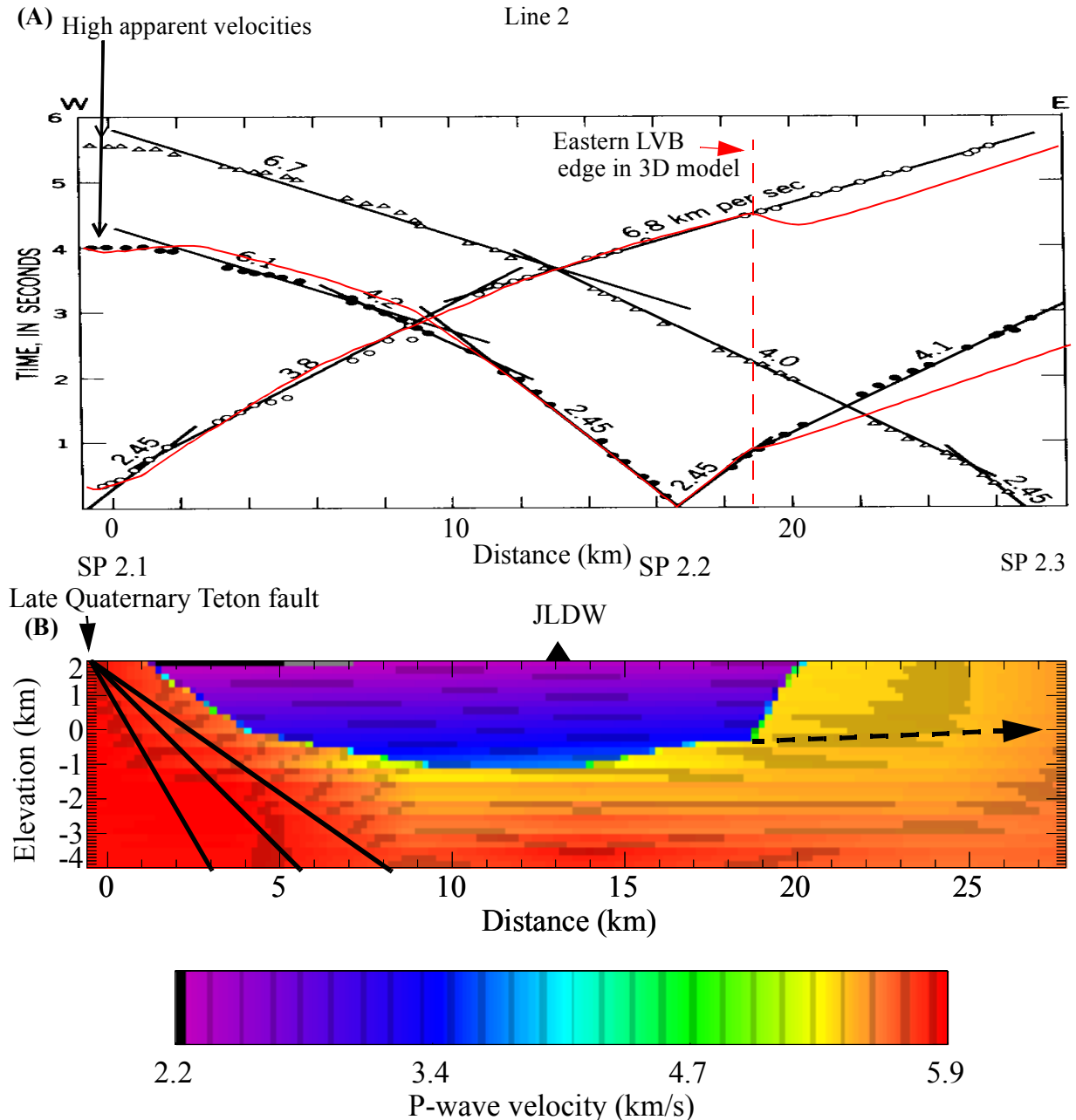


Figure 4-13: (A) P-wave travel-time plot for line 2 from Behrendt et al. (1968) and (B) corresponding slice of the 3D P-wave velocity model. Labeling of (A) is as in Figure 4-2. The western portion of line 2 located ~1 km north of Jenny Lake shows very-high apparent velocities for shotpoints 2.2 and 2.3 as shown by the black arrows. The red curves on line 2 are P-wave travel-time curves from the 3D velocity model (Figure 4-1) for shotpoints 2.1 and 2.2. The 0.1 s delay on the ~6.1 km/s apparent velocity western traveltime branch for shotpoint 2.2 suggests that the deepest portion of the LVB in the 3D model is 0.2-0.3 km too deep to fit the refraction data (see Figure 4-14). The lack of a travel-time advance in the refraction data along the eastern traveltime branch from shotpoint 2.2 indicates that the LVB continues east of the limit indicated by the 3D model, as shown by the dashed black arrow in (B); the refraction data show that ~2-km-thick low velocities persist to at least the eastern limit of line 2. The Teton fault is shown for dips of 35°, 45°, and 60° by the black lines in (B).

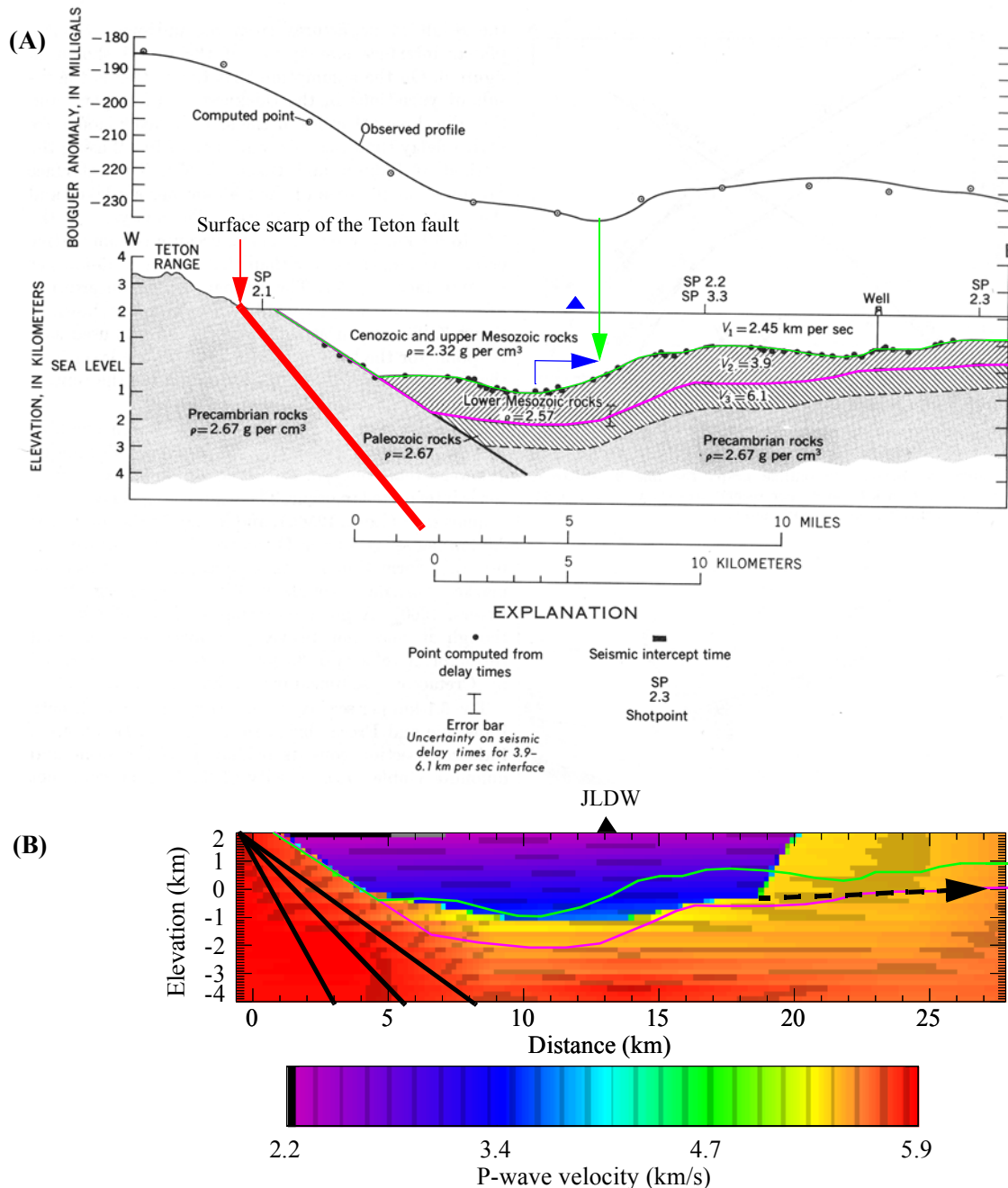


Figure 4-14: (A) Line 2 interpretation from Behrendt et al. (1968) and (B) corresponding slice of the 3D P-wave velocity model. Labeling of (A) is as in Figure 4-3. The lack of a travel-time advance in the refraction data along the eastern travelttime branch from shotpoint 2.2 (Figure 4-13) indicates that the LVB continues east of the limit indicated by the 3D model, as shown by the dashed arrow in (b); the refraction data show that ~2-km-thick low velocities persist to at least the eastern limit of line 2. The green curves in (A) and (B) are the Behrendt et al. (1968) interfaces between slow sediments and faster Mesozoic rocks and the magenta curves in (A) and (B) are Behrendt et al.'s interface between Mesozoic rocks and basement rocks. There is strong agreement in the depth to a significant velocity contrast between the Behrendt et al. (1968) model and the 3D model for the portion of the LVB west of JLDW, but east of the JLDW, the 3D model places the strong velocity contrast near the interface between Mesozoic rocks and basement rocks in model of Behrendt et al. (1968).

et al. (1968). The 3D velocity model is consistent with the findings of Byrd et al. (1994) that significant vertical and horizontal velocity gradients exist within the LVB. The 3D velocity model is consistent with the total thickness of lower density rocks within the LVB, particularly with the relatively small increase of gravity east of the dam (except for the fact that the LVB is artificially truncated to the east, as indicated in Figure 4-15). Specifically, it appears likely that the dam is located over the deepest portion of the LVB, as indicated by the observed gravity in Figure 4-14a. The time delay between the LVB-edge S-waves and the direct S-waves in the two earthquakes (events 1 and 3) also support having JLDW located over the deepest portion of the LVB.

It would be necessary to model more earthquake responses at JLDW from earthquakes located east of the dam to better constrain the eastern extent of the LVB velocity model. Since the eastern portion of the LVB is located furthest from the Teton fault, it is less likely to produce LVB responses that are as strongly amplified at the dam as the LVB-edge S-wave produced along the western margin of the LVB. This issue is discussed in more detail in the next section.

4.4 Seismic LVB Responses to Teton Fault Earthquakes: Influence of LVB Structure

To illustrate the importance of the 3D velocity structure on seismic responses at the dam, low-frequency (< 1 Hz) reciprocity Green's functions (RGF) calculated using the 3D velocity-density model (for use in Section 6) are discussed here. As indicated in Figure 4-15, there are three portions of the LVB margin that are located 10-to-14 km from the dam and likely to produce high-amplitude, critically reflected/refracted LVB-edge S-waves at the dam. Two of the three portions of the LVB margin in the critical distance range from the dam are located along the eastern end of the LVB where LVB structure is most uncertain. For instance, the strongest S-wave horizontal arrivals at the dam for a point-source located at the base a 35-degree-dipping Teton fault at the northeast corner of the fault (Figures 4-16 and 4-17) are the LVB-edge S-waves produced along the northeast corner of the LVB (see F8 in Figure 4-15). However, if the northeastern edge of the LVB is actually located more than 14 km from the dam, the LVB edge will not produce high-amplitude LVB-edge S-waves at the dam. Instead the response may be more like those found in Figures 4-18 and 4-19 for a point source at the southeast corner of a 35-degree-dipping Teton fault, where total durations are much longer, and LVB-edge S-wave amplitudes do not always exceed direct S-wave amplitudes. However, the amplitudes of the secondary arrivals are rather

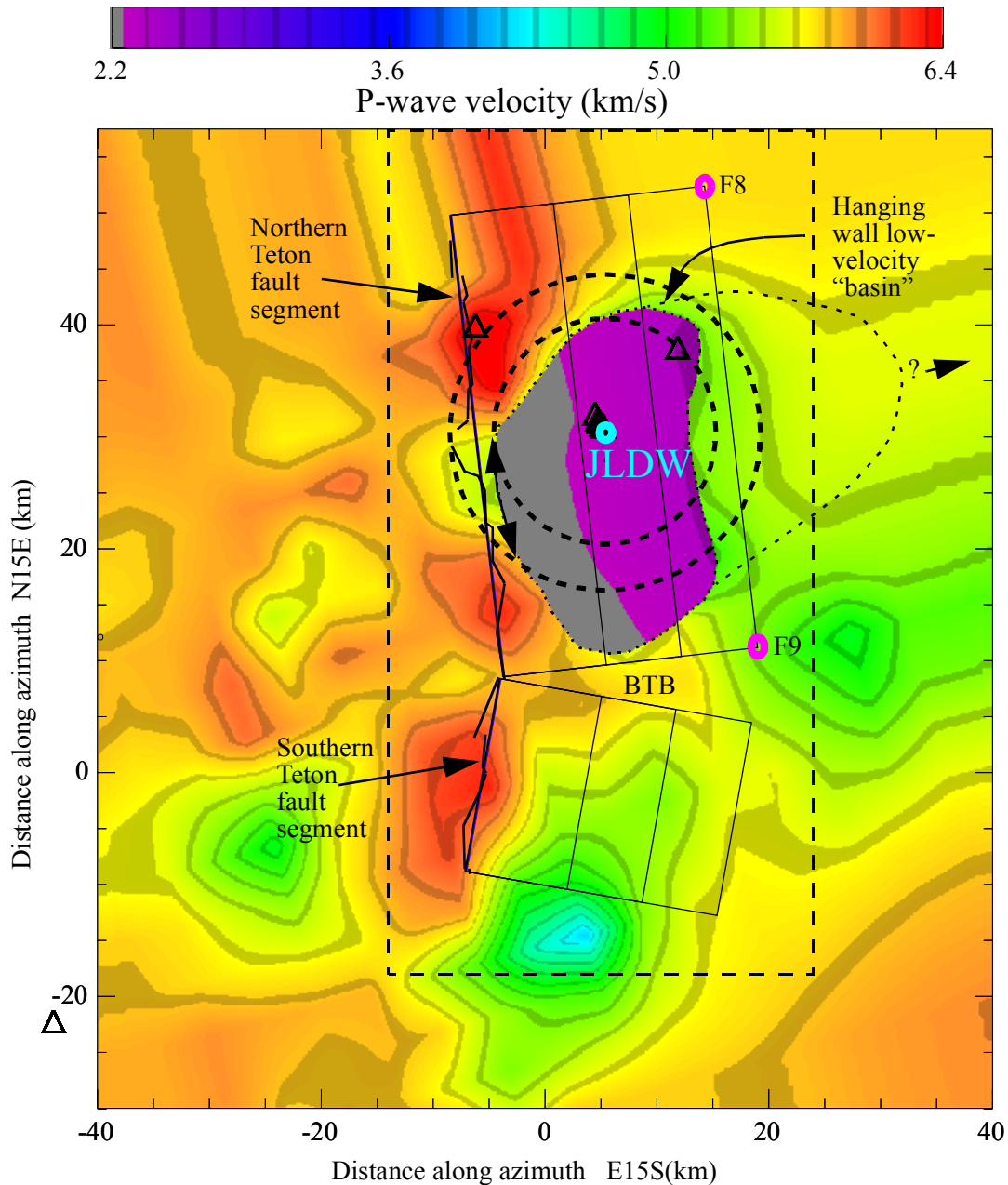


Figure 4-15: Plan view of the P-wave 3D velocity model with embedded Jackson Hole LVB at elevation 2 km. The postulated LVB is “closed”; it’s surrounded by high-velocities everywhere (in depth and plan views), however as indicated by the short-dashed black curve, question mark, and arrow, the eastern portion of the LVB is likely to extend well beyond the LVB indicated in the 3D velocity model. The plan projection of the idealized geometries of the two primary (northern and southern) segments of the Teton fault for dips of 35°, 45°, and 60° are the solid rectangles (surface trace to the left). Blue circle is the JLDW rock site station. The dashed rectangle shows the limits of the 3D finite-difference grid. Numbered magenta circles are point-source positions for Figures 4-16 and 4-17 (F8) and 4-18 and 4-19 (F9). Blacktail Buttes is denoted by BTB. The region between the thick dashed lines indicates the distance range from station JLDW that strong LVB-edge S-wave arrivals are produced. The double arrow line indicates the portion of the western LVB that acts as a strong secondary source of S-waves at the dam.

E15S horizontal component

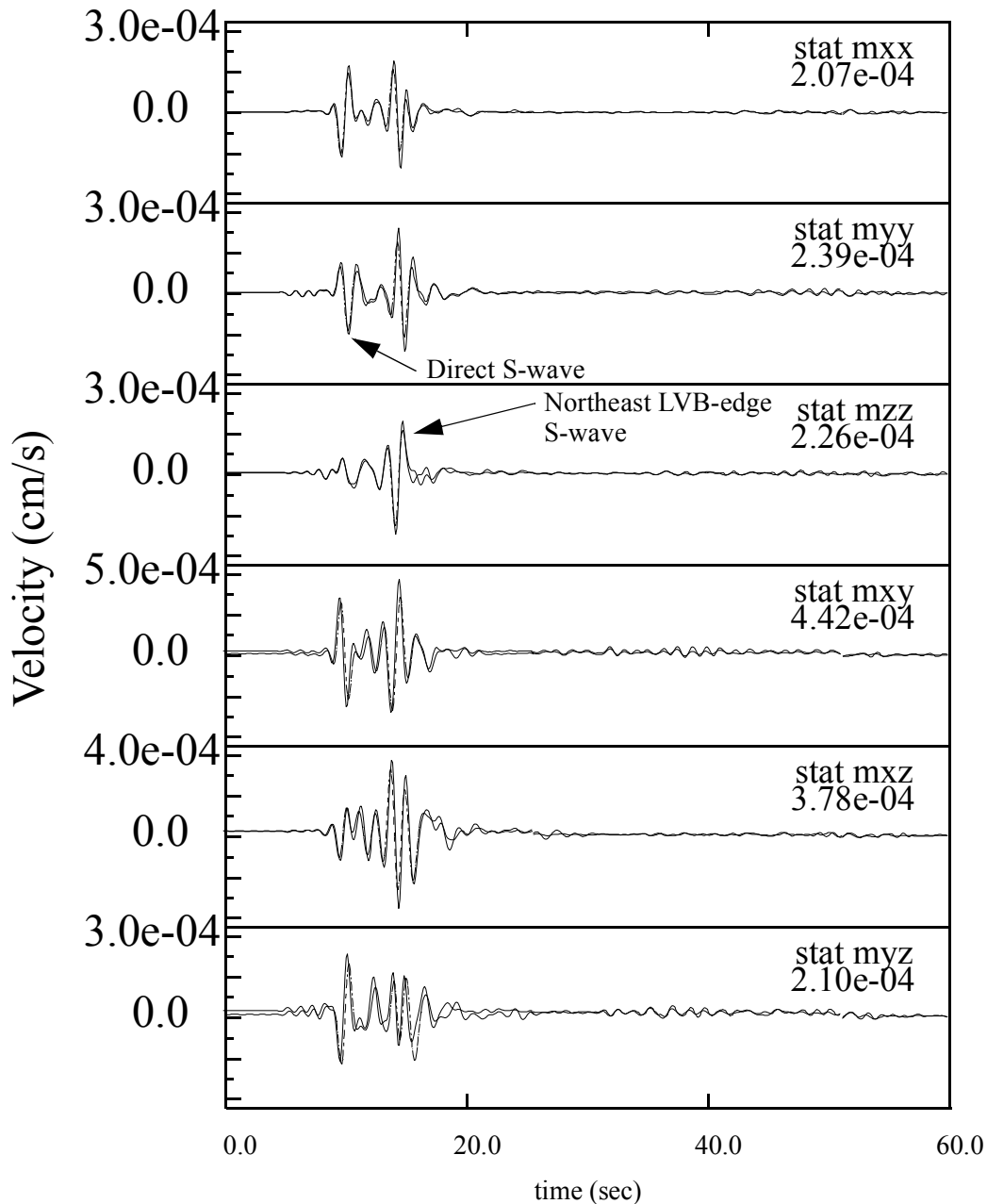


Figure 4-16: E15S horizontal component < 1 Hz 3D finite-difference RGF's moment-time histories at JLDW for a point-source at the northeast corner of the Teton fault. The point-source has a moment of 10^{20} dyne-cm (magenta circle labeled F8 on Figure 4-15). The mxx, mzz, and mxz moment components are most relevant for normal-faulting ground motions associated with the Teton fault. There are two seismograms shown for each moment component to illustrate the differences between the Graves (1996) and Graves and Day (2003) approaches to accounting for attenuation. The Graves and Day (2003) approach was used for all calculations in this report.

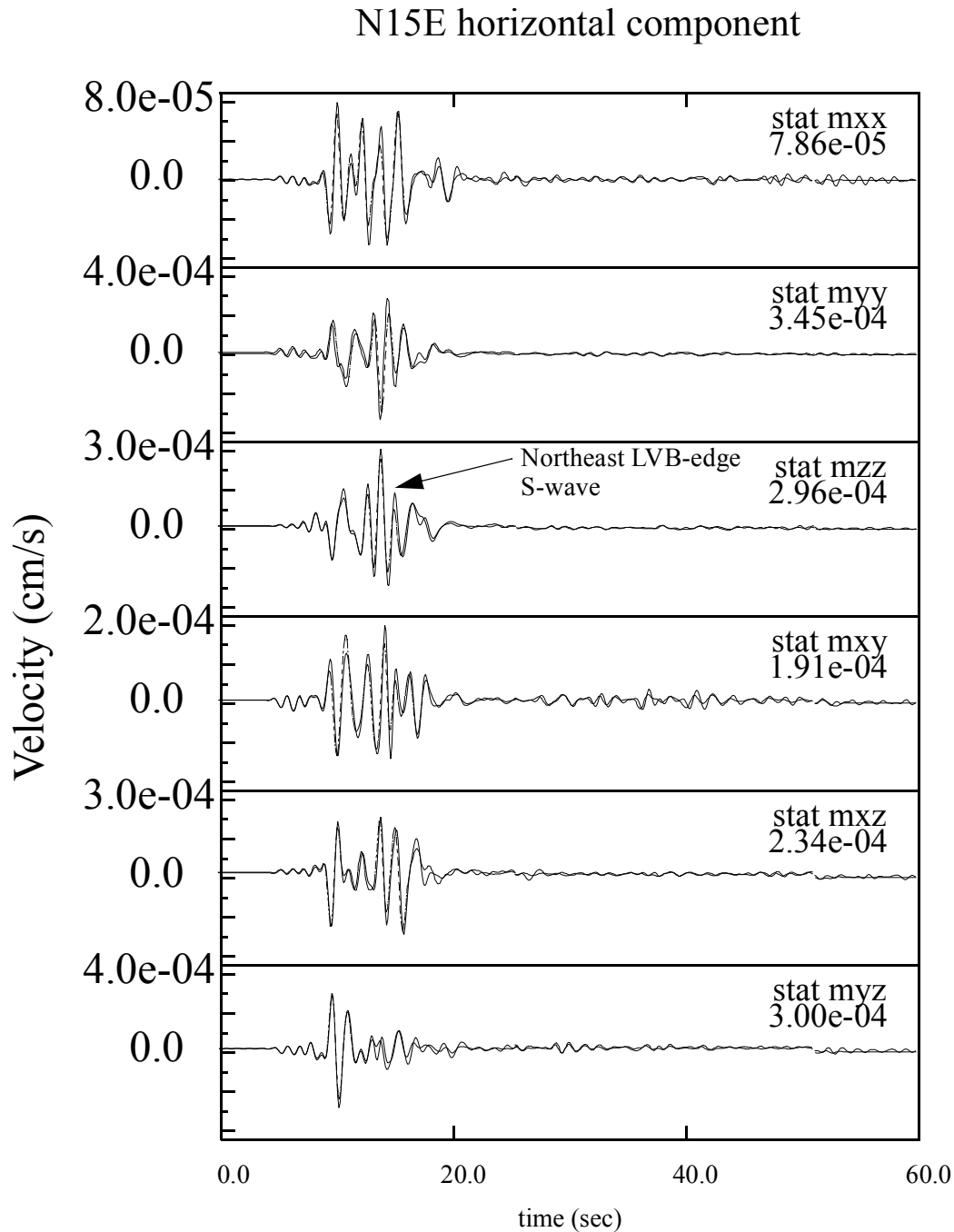


Figure 4-17: N15E horizontal component < 1 Hz 3D finite-difference RGF's moment-time histories at JLDW for a point-source at the northeast corner of the Teton fault. The point-source has a moment of 10^{20} dyne-cm (magenta circle labeled F8 on Figure 4-15). The mxx, mzz, and mxz moment components are most relevant for normal-faulting ground motions associated with the Teton fault. There are two seismograms shown for each moment component to illustrate the differences between the Graves (1996) and Graves and Day (2003) approaches to accounting for attenuation. The Graves and Day (2003) approach was used for all calculations in this report.

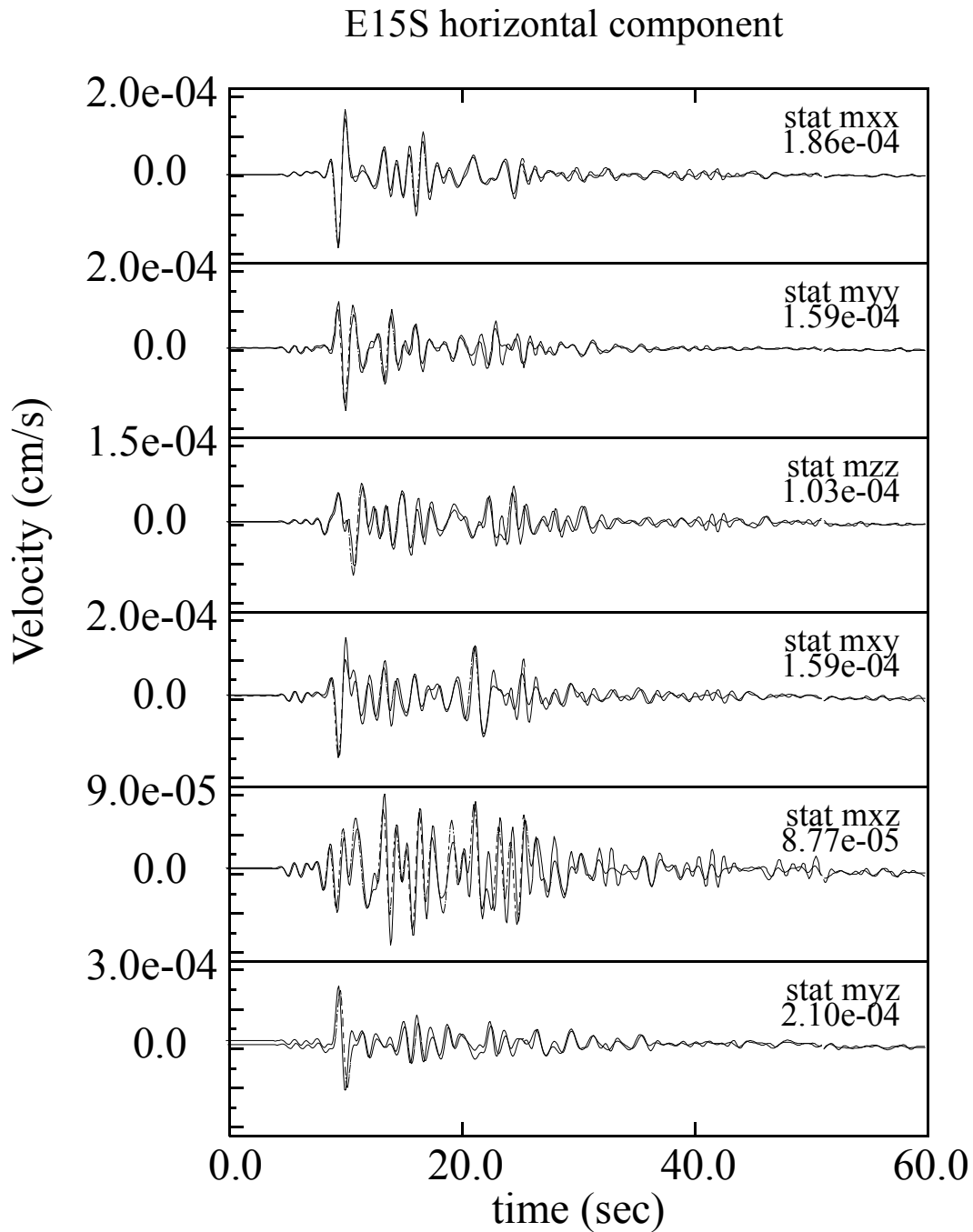


Figure 4-18: E15S horizontal component < 1 Hz 3D finite-difference RGF's moment-time histories at JLDW for a point-source at the southeast corner of the Teton fault. The point-source has a moment of 10^{20} dyne-cm (magenta circle labeled F9 on Figure 4-15). The mxx, mzz, and mxz moment components are most relevant for normal-faulting ground motions associated with the Teton fault. Note the longer duration of these moment responses relative to Figure 4-16. There are two seismograms shown for each moment component to illustrate the differences between the Graves (1996) and Graves and Day (2003) approaches to accounting for attenuation. The Graves and Day (2003) approach was used for all calculations in this report.

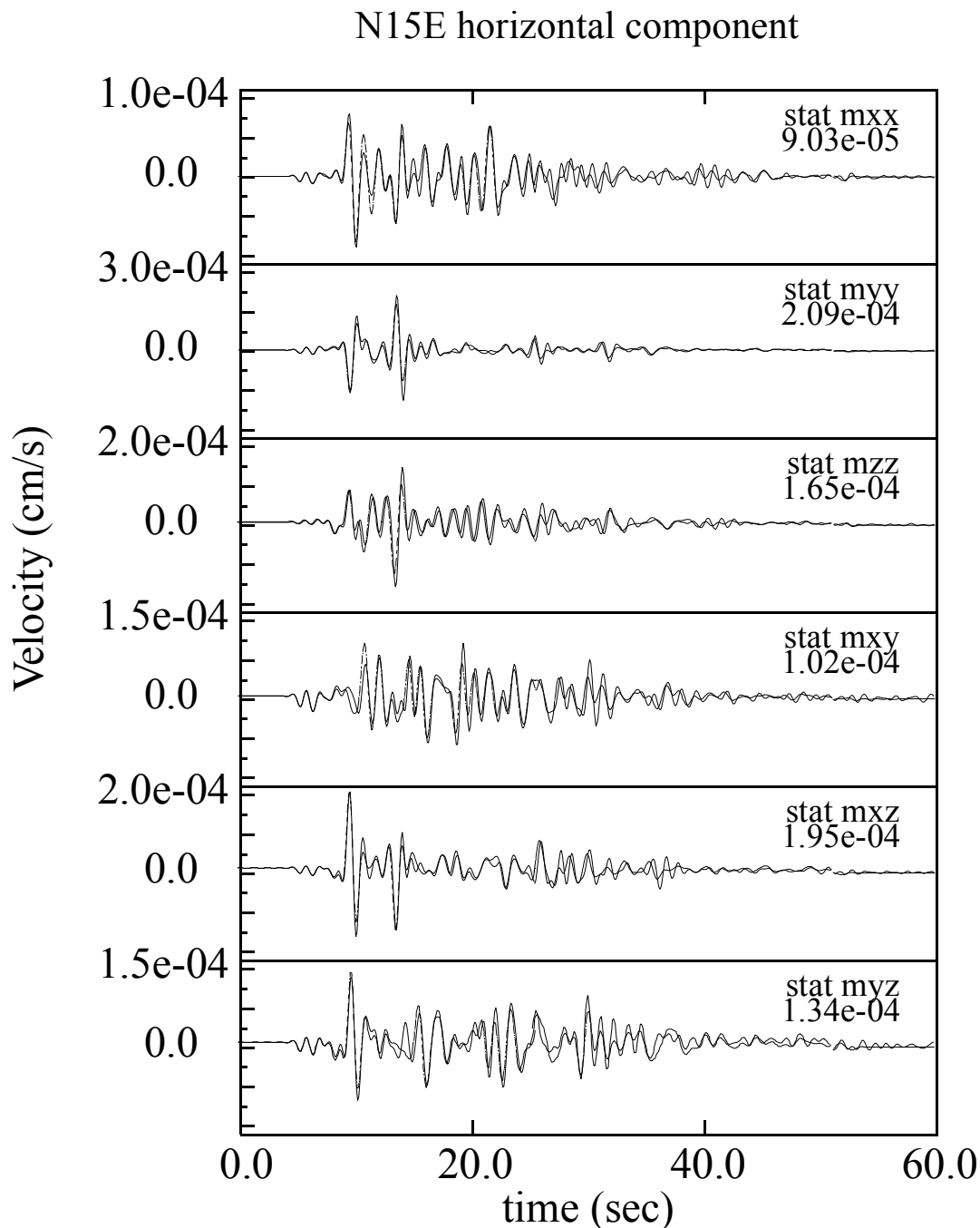


Figure 4-19: N15E horizontal component < 1 Hz 3D finite-difference RGF's moment-time histories at JLDW for a point-source at the southeast corner of the Teton fault. The point-source has a moment of 10^{20} dyne-cm (magenta circle labeled F9 on Figure 4-15). The mxx, mzz, and mxz moment components are most relevant for normal-faulting ground motions associated with the Teton fault. Note the longer duration of these moment responses relative to Figure 4-17. There are two seismograms shown for each moment component to illustrate the differences between the Graves (1996) and Graves and Day (2003) approaches to accounting for attenuation. The Graves and Day (2003) approach was used for all calculations in this report.

remarkable considering that the direct S-wave propagation distance is less than the half propagation distances of most LVB-edge S-waves. A nearly 10-km-long region of the along western margin of the LVB (Figure 4-15) provides a large secondary source dimension which explains why the amplitudes of LVB-edge S-waves are nearly comparable to direct S-wave amplitudes in (Figures 4-18 and 4-19). The longer durations in Figures 4-18 and 4-19 relative to Figures 4-16 and 4-17 also reflect the fact that the southern end of the LVB is located > 15 km from the dam, allowing LVB-edge surface waves to fully develop between the southern LVB-edge and the dam. If the LVB is extended further east and northeast, then the responses at the dam for seismic energy radiated from the northeast portion of the fault will likely be much longer than in Figures 4-16 and 4-17, but LVB-edge S-wave amplitudes should be somewhat reduced.

These results illustrate some of the sensitivities of seismic responses at the dam to assumed 3D velocity structure. To provide an overview of the influence of the 3D LVB on strong motion responses, E15S profiles of ground motion attributes, including Arias Intensities, are shown in Figure 4-20 for a kinematic simulation of a **M** 7.1 earthquake on the northern segment of a 35°-dipping Teton fault that extends to 16 km depth. Arias Intensity is a ground motion parameter that quantifies the potential destructiveness of an earthquake as the integral of the square of the acceleration-time history (Kayen and Mitchell, 1997). Arias Intensity correlates well with several commonly used engineering demand measures of structural performance, liquefaction, and seismic slope stability (Kayen and Mitchell, 1997). The kinematic rupture model for Figure 4-20 uses a different random seed to generate the asperity distribution than the rupture models used to produce Figure 6-11. The substantial differences in peak velocities and accelerations between Figures 4-20 and 6-11 illustrate the sensitivity of ground motions to details of fault rupture in the near fault region.

Peak ground motions and Arias Intensities are largest in the western half of the LVB, return to peak levels comparable to the hanging wall near the fault, at the position of the dam, and decrease past the dam in the E15S direction. Peak motions in the LVB east of the dam are less than peak motions on the hard-rock sites (> 3 km/s S-wave velocities) located west of the LVB adjacent to the fault. Unlike the western 8 km of the LVB, the dam is not subjected to extreme amplification associated with combined effects of rupture directivity and LVB amplification. However, the peak

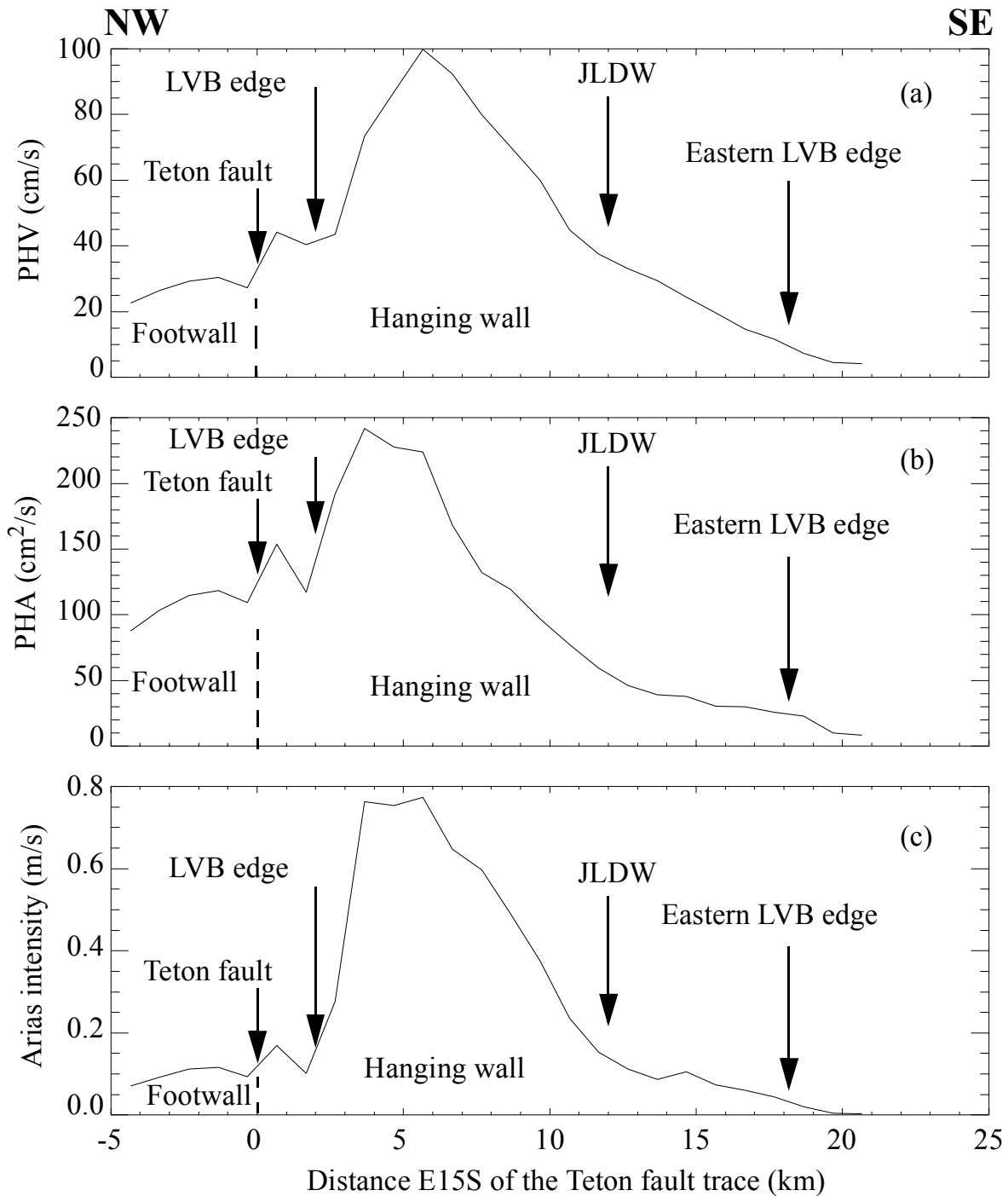


Figure 4-20: Simulated peak motion characteristics for a **M** 7.1 earthquake on the Teton fault. Long-period (**< 1 Hz**) peak horizontal velocities (PHV) (a), peak horizontal accelerations (PHA) (b), and Arias Intensities (c) for a profile of sites oriented E15S through the JLDW from a 3D finite-difference simulation of a **M** 7.1 normal-faulting earthquake on the northern Teton fault segment with a 35°-dip extending to 16 km depth. The hypocenter was located at 15 km depth, 2 km from the south end of the fault segment. The Jackson Lake LVB is located on the hanging wall, 2 km from the surface trace of the Teton fault.

velocities and Arias intensities at the dam are larger than at sites located adjacent to the fault on the high-velocity portion of the hanging wall, indicating that the dam is subjected to amplification associated with rupture directivity; rupture directivity is smaller at the dam for fault dips of 45° and 60° , as shown in Section 6. Amplification at the dam is a result of it being located in the LVB. Note that high-velocity hard-rock footwall peak horizontal velocities (PHV) are $< 1/4$ of the largest PHV's in the LVB (1/16th of the LVB's peak kinetic energy), footwall peak horizontal accelerations (PHA) are $< 1/2$ of maximum LVB PHA's, and footwall Arias Intensities are $< 1/7$ th of the maximum LVB Arias Intensities. PHA's, PHV's, and Arias Intensities diminish to values less than high-velocity footwall site values about 3 km east of the dam, indicating the absence of rupture directivity for sites located > 15 km east of the fault. The results in Figure 4-20 represent but one kinematic rupture simulation, so it's important to not over interpret the results. However, Figure 4-20 provides a good schematic example of systematic spatial variations of strong motions relative to the surface scarp of the Teton fault and the LVB. Section 6 presents detailed calculations focused on quantifying strong motion responses at JLDW.

Stirling et al. (2002) postulate that rock site observations of balanced rocks may provide paleo ground motion information. Stirling et al. (2002) compared observed balanced-rock-site amplifications with observed soil-site responses. They found that 1 Hz rock site responses were half those of soil sites. Yet Stirling et al. (2002) concluded that since 10 Hz responses were comparable, rock sites responses were not substantially different than soil sites. However, Stirling et al. (2002) fail to acknowledge that peak velocities (~ 1 Hz response) provide better correlations with earthquake damage than peak accelerations (~ 10 Hz responses) (EERI, 1994). Also, ground motion durations and thereby, integral measures, such as Arias Intensity, that correlate much better than peak accelerations with earthquake damage (Kayen and Mitchell, 1997), will be lowest at rock sites (see Figure 4-20c). Given all these caveats about Stirling et al. (2002), and the low-frequency ground motion results in Figure 4-20, is it reasonable to expect normal-faulting, near-fault footwall proxies for paleo-ground motions to have any relevance to ground motions in hanging wall LVBs adjacent to normal faults? Probably not, given the contrast between low Arias Intensities adjacent to the fault in the footwall, and Arias Intensities seven times larger in the LVB at sites located > 5 km from the fault (Figure 4-20c). It is clear that footwall paleo ground motion proxies are not realistic ground motion proxies for hanging wall ground motions for typical

normal fault crustal velocity geometries, including the crustal velocity structure adjacent to the Teton fault.

4.5 Structural Interpretation of Hanging Wall Geology and Geophysics

The late-Quaternary surface scarp of the Teton fault is located ~1-2 km west of the western margin of the LVB as constrained by seismic refraction and gravity data (Figures 4-13 to 4-15). Line 2 shotpoint 2.1 is located about ~0.5 km east of the Teton fault scarp (Figure 4-14). The high-apparent velocities near shotpoint 2.1, the high-apparent velocities that extend 3 km east of the western edge of line 2 for shotpoint 2.2 travel-times, and gravity modeling of Lavin and Bonini (1957), Behrendt et al. (1968), and profile 2 of Byrd et al. (1994) clearly show that high velocities and high densities persist at shallow depths ~1-2 km east of the surface scarp of the Teton fault in the vicinity of Jenny Lake (Figures 4-13 and 4-14). The gravity interpretations of Byrd et al. (1994) for profiles north (profile 1) and further south of Jenny Lake (profile 3) fail to satisfy maximum gravity observations located immediately east of the surface scarp of the Teton fault, because low-density LVB sediments with thickness of ~2 km are extended west by Byrd et al. (1994) to abut the present-day Teton fault scarp. A more parsimonious interpretation of Byrd et al.'s (1994) gravity profiles 1 and 3 would extend high-density material 1-2 km east of the late-Quaternary surface scarp of the Teton fault to satisfy the maximum gravity amplitudes observed immediately **east** of the Teton fault scarp on each of the profiles. Thus, it appears that the low-velocity, low-density LVB begins >1 km east of the late-Quaternary scarp of the Teton fault for most of the length of the northern Teton fault segment (Figure 4-15). This means that both the footwall and hanging wall in the vicinity of the Teton fault consist of relatively high-density and high-velocity materials; the LVB does not represent the hanging wall interface of the active Teton fault. This has some important ground motion and rupture dynamic implications that are discussed in Section 6.

The high-velocity, high-density structure on each side of the Quaternary surface trace of the Teton fault was noted by Behrendt et al. (1968) and Byrd et al. (1994), among others. Several investigators have postulated the existence of a second normal fault bounding the western margin of the LVB (Lavin and Bonini, 1957; Behrendt et al., 1968; Tibbetts et al., 1969). Byrd et al. (1994) discount the existence of a normal fault bounding the LVB (e.g., > 1 km east of the late-

Quaternary Teton fault scarp), and appeal to the existence of a Laramide or older structure high-density body along the northern 40 km of the Teton fault to explain the high gravity amplitude observations east of the mapped surface trace of the Teton fault. An enigmatic aspect of the postulated normal fault several km east of the late Quaternary scarp of the Teton fault, is its lack of apparent Quaternary activity (Gilbert et al., 1983; Susong et al., 1987; Smith et al., 1993; Byrd et al., 1994; Byrd, 1995) and its relatively shallow dip of about 30 degrees (Behrendt et al. 1968, Figure 4-14). The 10-degree, west-side-down tilt of the Teton Range in response to normal-faulting, as inferred by Byrd et al. (1994) from paleomagnetic data, provides a mechanical explanation for the westward migration of the Teton fault into the Teton Range and the existence of multiple normal faults. A westward tilt of 10 degrees would take a 40-degree east-dipping normal fault and rotate it to 30 degrees. Mandl (2000, p. 333-334) showed that as a normal fault approaches 30 degrees it becomes mechanically impossible to continue normal fault growth, particularly if fault growth is controlled by processes below 10 km. Consequently, in response to the westward tilting in the vicinity of the Teton Range, the Teton fault jumped west several km and initiated a new more steeply dipping ($> 35^\circ$), east-dipping normal-fault in its present position.

Buck (1993) showed isostatic responses make it likely that normal faults will tend to rotate toward shallower dips as total fault displacement increases. Collettini and Sibson (2001) use worldwide focal mechanism data from $M > 5.5$ earthquakes to show that the most common normal fault dips are 40-to-45 degrees, substantially lower dips than would be ascribed to normal faults based on simple faults mechanics of Anderson (1951) of 60-to-75 degrees. Thus, even if the initial dip of the late-Quaternary scarp of the Teton fault was 60° several m.y. ago, the results of Buck's (1993) analyses indicate that the present dip of the active Teton fault is likely to be < 50 degrees. The preponderance of normal faulting dips ≤ 50 degrees (76%) in Collettini and Sibson (2001) also suggests that the dip of the currently active trace of the Teton fault is likely to be $\leq 50^\circ$. As noted in Section 2, there appears to be a third set of normal faults developing west of the primary late-Quaternary Teton fault scarps shown on Figure 4-15. These western-most normal faults have relatively small late-Quaternary scarp heights of < 10 m, but steep dips of $\sim 75^\circ$, consistent with the development of new normal faults at high angles predicted by fault mechanics (e.g., Anderson, 1951).

Westward tilt of the Teton Range (Byrd et al., 1994) and isostatically-driven progressive fault rotation toward shallower dips with fault displacement (Buck, 1993) explains the existence and current orientations of all three “Teton” faults, a now inactive $\sim 30^\circ$ -dipping relic Teton fault bordering the western margin of the LVB, the currently late-Quaternary-active range-front-bounding Teton fault that has produced multiple surface-rupturing earthquakes in the past 17-18 ka (Section 2), and an incipient steeply-dipping Teton fault developing several km west of the range front that is characterized by relatively small-offset fault scarps (Section 2). In summary, the existence of three “Teton” faults, each offset from its neighbor by several km in the east-west direction, is consistent with fault mechanics, all the geophysical and geological data, including the lack of Quaternary activity on the eastern fault, and expected isostatic responses. The ground motion investigations in the report focus exclusively on earthquake rupture scenarios on the range-front Teton fault (Figure 4-15); earthquake scenarios are not considered for the other two “Teton” faults because the easternmost fault shows no signs of late-Quaternary activity (Gilbert et al., 1983; Susong et al., 1987; Smith et al., 1993; Byrd et al., 1994; Byrd, 1995) and the western most fault is located further from the dam, and would produce smaller ground motions at the dam.

The horizontal offset of the hanging wall LVB several km east of the presently-active Teton fault is typical of most normal faults in the Wasatch fault zone region of the intermontane seismic belt (ISB) (Zoback, 1983). It may be that fault rotation and migration of normal faults into the footwall (into range fronts) may be the norm in the ISB. Zoback (1983) only reports three cases in a sample of 23 normal faults in the Wasatch fault zone that consists of a single normal fault bounding the hanging-wall LVB. The rest of the normal fault hanging wall LVB in Zoback (1983) contained at least one normal fault embedded in the LVB.

4.6 Conclusions

The refraction data and MEQ waveform modeling indicate that nearly linear vertical and horizontal velocity gradients characterize the LVB generally referred to as Jackson Hole, consistent with the seismic refraction interpretations of LVB velocity structure of Byrd et al. (1994). Behrendt et al.'s (1968) and Tibbetts et al. (1969) interpretations of the refraction data used constant velocity layers with strong velocity discontinuities within the LVB; these models fail to reproduce strong broadband arrivals that follow direct S-waves by ~ 3 -6 s. These arrivals

are composed of S-waves and surface waves produced at the LVB margins. The 3D velocity model of the LVB developed in this section is similar to the velocity model of Byrd et al. (1994) and reproduces observed seismograms from three earthquakes located near the edges of the LVB quite well. The paucity of strong S-P conversions on vertical-component seismograms from station JLDW, also argues against the existence of strong velocity discontinuities internal to the LVB, postulated by Behrendt et al. (1968). Geophysical P- and S-wave velocity logs near station JLDW (Sirles, 1986) provided near-surface S-wave velocity estimates that were consistent with observed LVB-edge S-wave and surface wave travel-times to the LVB rock site.

The 2D finite-difference waveform modeling presented in this section shows that earthquake seismograms recorded at station JLDW inside the LVB can constrain LVB margin locations and dip geometries using earthquakes located near LVB edges, and independent constraints on earthquake locations and focal mechanisms provided by a large-scale Jackson Lake seismographic network. The JLSN provided the data necessary to constrain earthquake locations, focal mechanisms, and large-scale 3D P-wave velocity structure, and made it possible to model broadband earthquake recordings in the LVB to constrain Jackson Lake LVB P- and S-wave velocity structure. The gravity data in Behrendt et al. (1968) and Byrd et al. (1994) provided valuable information to interpolate LVB margin structure between constraints provided by the 2D finite-difference modeling and seismic refraction data, but interpretation of the gravity data is intrinsically non-unique.

While the 3D model of the LVB appears to provide a good representation of western LVB velocity structure close to the Teton fault, the 3D LVB model is clearly artificially truncated east of the dam (Figure 4-13). It would be necessary to perform 2D or 3D seismogram modeling of LVB recordings of earthquakes east of the dam to constrain the LVB velocity structure > 8 km east of the dam. It's logical that eastern LVB velocity structure is less important than western LVB structure, because the Teton fault interacts more strongly with the western LVB. It is not clear how significantly the artificial truncation of the LVB influences estimated ground motions at the dam. For instance, the LVB-edge S-wave amplitudes in Figures 4-16 and 4-17 may be overestimated, but the total ground motion durations may be underestimated if the eastern margin

of the LVB extends > 4-to-5 km further east than indicated in Figure 4-15. This issue probably warrants further investigation.

The seismogram modeling of microearthquakes shows that 3D velocity-model Green's functions are necessary to simulate ground motions within the LVB, not just to obtain realistic durations, but to include the constructive interference effects of coherent secondary sources, like LVB-edge *S*-waves. Empirical Green's functions may underestimate 1-4 Hz responses because the coherent LVB-edge *S*-waves are probably not adequately represented by the eight empirical Green's functions used in Section 6. As Figure 4-20 shows, near-surface ground motion amplitudes may be very large along the western margin of the LVB due to rupture directivity. Thus, material nonlinearity may occur at the LVB edges; nonlinearity may modify LVB-edge *S*-wave and surface contributions to LVB ground motions. It may be important to conduct 2D P-SV plane-wave experiments using nonlinear finite-difference or finite-element codes to ascertain if near-surface, LVB-edge nonlinearity substantially influences ground motion durations and amplitudes within the LVB.

Since the majority of ground motions used to develop ground motion attenuation relations are from California, it's important to recognize the significant differences between the crustal velocity structure near the Teton fault and typical California crustal velocity structure. Near-surface P-wave velocities are ~6 km/s near the surface adjacent to the Teton fault. In southern California, P-wave velocities of 6 km/s are typically not encountered until depths of 5-10 km (Hauksson and Haase, 1997). High basement velocities extending to near the surface in the vicinity of the Teton fault translates into very large velocity contrasts between the LVB and surrounding basement rocks, particularly along the western half of the LVB. Thus, even though LVB *S*-wave velocities are similar to California "rock" or NEHRP site class B *S*-wave velocities (> 720 m/s), the JLDW rock site behaves more like California stiff-soil site with *S*-wave velocities of 300-to-600 m/s, than a California "rock" site. The large velocity contrasts between the LVB and the basement rock makes the LVB a strong collector of radiated seismic energy (Figure 4-7a), which produces unusually long observed durations at JLDW (Section 5), long synthetic ground motion durations (Figures 4-16 and 4-17) and amplification of ground motions within the LVB (Figure 4-20).

Seismographic network monitoring by the JLSN for over 16 years was necessary to record a large number of earthquakes and associated arrival time data to constrain 3D crustal velocity structure. Since earthquakes tend to cluster in space and time (Section 3), a long duration of seismic monitoring was required to begin to fill the 3D volume of the crust with earthquakes. It's necessary to have earthquakes distributed throughout the 3D crustal volume to obtain reasonable constraints (ray-path coverage) on 3D velocity structure. The five-year duration of broadband site-response monitoring was critical to obtaining earthquakes located on-or-near the Teton fault, given the relatively low-rate of seismicity observed on the Teton fault trace and other major ISB normal faults; one of the earthquakes used in the seismogram modeling of LVB velocity structure occurred in Sep. 1996 and another occurred in Nov. 2001. Longer duration broadband three-component monitoring of site responses increases the probability of recording larger-magnitude earthquakes that could provide the data necessary for modeling seismograms to lower frequencies than could be accomplished with the site-response data available for this study. The configuration of the JLSN provided the supplemental data necessary to constrain earthquake locations and focal mechanisms; seismogram modeling cannot constrain LVB velocity structure when there are too many unconstrained parameters, like earthquake locations, focal mechanisms, and large-scale 3D velocity structure. The absence of three-component broadband seismographic stations on the periphery of the LVB limited resolution of the characteristics of LVB boundary structure and precluded absolute amplitude calibration of LVB responses.

The 3D velocity model developed here provides a basis to use 3D finite-difference methods to synthesize strong ground motions at Jackson Lake Dam. It would be prudent to investigate the significance of several aspects of the 3D model on ground motion predictions at the dam. Modeling of broadband site-response recordings of earthquakes located east of the dam would help constrain the extent and velocity structure of the eastern limits of the LVB. Longer duration broadband site response and seismographic network monitoring would likely provide larger-magnitude earthquake recordings with sufficient signal-to-noise properties to allow 3D (instead of 2D) finite-difference seismogram modeling of LVB structure for frequencies on the order of 1 Hz.

This section has focused on the 3D velocity structure of the Jackson Hole LVB and seismic responses at the ~ 1 km/s near-surface S-wave velocity station JLDW, located just south of

Jackson Lake Dam. A portion of the dam is located on a very-low-velocity (VLV) glacial scour basin, with near-surface S-wave velocities < 100 m/s. The next Section focuses on empirical and synthetic seismogram analyses of the seismic responses of the VLV glacial scour basin and the reference rock station JLDW.